

# A $T_2 \times R^2$ roadmap to Confinement in SU(2) Yang-Mills theory

---

Georg Bergner<sup>a</sup> Antonio González-Arroyo<sup>b,c</sup> Ivan Soler<sup>d</sup>

<sup>a</sup>University of Jena, Institute for Theoretical Physics,  
Max-Wien-Platz 1, D-07743 Jena, Germany

<sup>b</sup>Instituto de Física Teórica UAM/CSIC, Nicolás Cabrera 13-15,  
Universidad Autónoma de Madrid, E-28049 Madrid, Spain

<sup>c</sup>Departamento de Física Teórica, Módulo 15,  
Universidad Autónoma de Madrid, Cantoblanco, E-28049 Madrid, Spain

<sup>d</sup>Dipartimento di Fisica dell'Università di Pisa and INFN,  
Largo Pontecorvo 3, I-56127 Pisa, Italy

E-mail: [georg.bergner@uni-jena.de](mailto:georg.bergner@uni-jena.de), [A.Gonzalez-Arroyo@pm.me](mailto:A.Gonzalez-Arroyo@pm.me),  
[ivan.soler@df.unipi.it](mailto:ivan.soler@df.unipi.it)

ABSTRACT: We study the behaviour of SU(2) Yang-Mills fields on a  $T_2 \times R^2$  geometry where the two-torus is equipped with twisted boundary conditions. We monitor the evolution of the dynamics of the system as a function of the torus size  $l_s$ . For small sizes the behaviour of the system is well understood in terms of semiclassical predictions. In our case, the long distance structure is that of a two-dimensional gas of vortex-like fractional instantons with size and density growing with  $l_s$ . Our lattice Monte Carlo simulations confirm the semiclassical predictions and allow the determination of the relevant scale signalling the transition to the non-dilute situation. At low densities the string tension takes the standard value of a 2D center-vortex gas, growing with the density and approaching the value measured at infinite volume. Our work includes preliminary studies of the extension to SU( $N$ ) and to the region of large sizes in which boundary conditions are irrelevant, and all physical scales are determined by the  $\Lambda$  parameter.

---

## Contents

<b>1</b>	<b>Introduction</b>	<b>2</b>
<b>2</b>	<b>The semiclassical regime on <math>T_2 \times R^2</math></b>	<b>5</b>
2.1	Generalities about the semiclassical approximation	5
2.2	Classical solutions	6
2.3	Description of the semiclassical components	10
2.4	Properties of the 2D gas of FI and AFI	11
2.5	Role of twist and of ordinary $Q = 1$ instantons	14
2.6	Scaling of the densities and the continuum limit	15
<b>3</b>	<b>Ensemble generation and numerical analysis</b>	<b>16</b>
3.1	Monte Carlo simulations	17
3.2	Gauge noise filtering	18
3.3	Fitting topological structures	20
3.4	Characterizing the distributions	22
3.5	The identification algorithm	26
<b>4</b>	<b>Analysis of Results</b>	<b>27</b>
4.1	Poisson distributed 2D gas of vortex-like fractional instantons	27
4.2	Density evolution as a function of $\beta$	31
4.3	Relation with the string tension	33
4.4	Flow dependence of the results	35
<b>5</b>	<b>Going to larger torus sizes</b>	<b>39</b>
<b>6</b>	<b>Conclusions and future prospects</b>	<b>41</b>
<b>A</b>	<b>Dependence of the distributions on gradient flow parameters</b>	<b>48</b>
<b>B</b>	<b>Distribution of fit parameters at larger <math>N_c</math> (SU(3) and SU(4))</b>	<b>48</b>
<b>C</b>	<b>Further characteristics of fractional instanton distribution</b>	<b>49</b>
<b>D</b>	<b>Improved fit of fractional instanton distributions</b>	<b>50</b>
<b>E</b>	<b>Extra tables</b>	<b>51</b>

---

## 1 Introduction

In this paper, we study the behaviour of  $SU(N)$  Yang-Mills fields living on  $T_2 \times R^2$ , a four dimensional space in which two dimensions are compactified as a flat square torus equipped with twisted boundary conditions (TBC) [1–3]. Our purpose is to monitor the evolution of the system as a function of the linear size of the 2-torus measured in physical units. Since the theory is asymptotically free, we expect perturbative and semiclassical methods to be a good approximation to the system when the size is small, and by following the track towards large volumes we expect to gain insight into the complete understanding of the fascinating non-perturbative properties of the theory. Our numerical analysis considers mainly the gauge group  $SU(2)$ , while we also comment on generalizations to larger  $N$ .

This strategy has a long history. In the 90’s, a similar pathway was followed with an equivalent goal in mind. It was first explored by Lüscher [4] in the study of two-dimensional (2D) asymptotically free non-gauge field theories, and later extended to the case of a Yang-Mills system in four dimensions (4D) [5]. All these studies were done within a Hamiltonian type of setting, in which the euclidean time direction is non-compact while the spatial directions are compactified on a 3-torus whose size-dependence is being monitored ( $T_3 \times R$ ). One advantage is that one does not expect a phase transition to take place at a particular size separating the weak coupling region from the large volume one, and thus spoiling the connection one is trying to establish. Studies were done both with and without twisted boundary conditions using analytic [5–12] and numerical [13, 14] methods. It feels natural to consider TBC for various reasons. First of all, perturbative studies with periodic boundary conditions have to address the peculiar orbifold structure of the zero-energy configurations. These zero energy states (called *torons* in Ref. [15, 16]) are indeed the particular case of flat connections on the torus. Performing perturbative/semiclassical studies in this setting is a tour-de-force that some researchers, such as Pierre van Baal, had to address to pursue the program [7–9]. These problems are absent if suitable TBC are employed, and perturbative studies of the low energy states can be performed quite straightforwardly [10–12]. There is another very puzzling phenomenon related the volume dependence of the system that suggests the use of TBC. That is the fact that this volume dependence disappears at large  $N$ . Periodic boundary conditions fail to preserve the necessary center-symmetry for this phenomenon to take place [17, 18]. However, using TBC, one can enforce enough symmetry to attain volume independence [19]. How exactly this fact matches with the semiclassical program is still to be elucidated. In any case it is obvious that even at finite  $N$ , TBC helps enforcing center-symmetry and hence smoothens the path towards large volumes. Indeed, the studies performed on the 90’s focused on the glueball spectrum, showing that as the size is varied, level crossings occur in the low-lying spectrum for periodic boundary conditions that are absent for TBC [8].

However, even for the case of TBC, it soon became clear that one had to go beyond perturbation theory to connect small to large volumes: semiclassical methods are necessary. This is somehow related to the recovery of the spatial  $(Z(N))^3$  center-symmetry on  $T_3 \times R$ . The case of  $SU(2)$  is particularly simple, since in that case one finds that there are two gauge inequivalent zero-energy states, which are invariant under a  $Z(2) \times Z(2)$

subgroup. The remaining  $Z(2)$  group is broken spontaneously by choosing any of the two gauge inequivalent vacua (zero-energy states). However, there is no real breaking of this symmetry since it costs a finite amount of action to tunnel between both zero-energy states. The configuration with minimum action that tunnels between these vacua is indeed a fractional instanton with topological charge  $Q = 1/2$  [20, 21]. The situation resembles pretty much the problem of a 1-dimensional scalar field with a double well-potential. The finite action of the kink solution, which tunnels among the two minima, restores the symmetry, generating a mass-gap proportional to the exponential of this kink-action. For the Yang-Mills system the equivalent of the field is played by a particular Polyakov loop aligned along the direction of the 't Hooft magnetic flux, and the kink is replaced by the fractional instanton. Notice also that the role of the mass-gap is now the energy with the correlator of two of the particular Polyakov lines separated over time (an electric flux energy in 't Hooft terminology). However, the minimum energy associated with the exponential decay of the correlator of two Polyakov lines is what we associate with the string tension. For large volumes, the energy grows linearly with the size of the torus with a slope given by the string tension. This is what connects the semiclassical study to the recovery of the Confinement regime.

Indeed, a semiclassical study using similar formulas that we will use here was already performed in the 90's within that spatial volume dependence program on  $T_3 \times R$  [22, 23]. At small torus sizes, the system gives rise to a 1-dimensional gas of kink-like fractional instantons with a Poissonian distribution and whose density, controlled by the semiclassical formulas, grows with the spatial size. Remarkably, the analytic expressions matched with the numerical results obtained by a Monte Carlo analysis of the system using lattice methods. However, the lattice methodology allows us to explore the system all the way towards large volumes. Interestingly enough, for physical sizes that are not too far from the region where the dilute gas approximation breaks down, the electric flux energy dependence on the torus size flattens up to a linear one, giving values of the string tension close to those that other researchers had measured for the large volume string tension [23, 24]. In trying to understand this smooth transition, one of the present authors and his students proposed a mechanism to explain it [24, 25]. The main ideas are the following. At small volumes the size of the fractional instantons is fixed by the torus size. Semiclassical formulas include quantum corrections which imply that bigger fractional instantons have a higher probability (as is the case for instantons). However, this does not occur all the way to infinite size. At large enough sizes the most probable FI size and separation is a dynamical scale given in terms of the Lambda parameter of the theory. Hence, once the torus becomes larger than this size, fractional instantons do not grow and tend to fill in the full four dimensional space. This then explains how the system recovers rotational invariance and the twisted boundary conditions on the 3-torus become irrelevant. Effectively, the resulting picture of the vacuum is described by the 4D fractional instanton liquid model (FILM). Such a liquid would induce and relate quantities, like the string tension, the topological susceptibility and the condensate, which appear unrelated in other scenarios. We point to a recent review [26] of the proposal including additional references. Some recent lattice gauge theory results has been argued to provide additional evidence in favor of the FILM model [27] (see

also Ref. [28]).

More recently, a new set of papers has explored a different roadmap with a similar strategy in mind. This originated in the rather complementary study of an  $S_1 \times R^3$  geometry and using the size of the short circle as a monitoring parameter to connect the region of weak coupling towards the strongly-coupled fully infinite volume one. It is important that this evolution is free of phase transitions. The connection is then smooth: a process that has been labelled *adiabatic continuity* [29, 30]. One possible way to prevent phase transitions is to focus on gauge theories with adjoint fermions: Adjoint QCD. It is known that the gluonic interactions induce the Polyakov loop to concentrate on elements of the center, effectively breaking the center symmetry and inducing a phase transition. Adjoint fermions act in the opposite direction and can neutralize the effect. This is clear for the case of  $\mathcal{N} = 1$  Supersymmetric Yang-Mills, at least when the boundary conditions are chosen periodic rather than antiperiodic to preserve supersymmetry [31]. The claim is that even for massive fermions this is indeed the case [32]. Another possibility explored is to deform the Yang-Mills interaction by adding double trace terms that give additional weight to the center-symmetric situations [33, 34]. This  $S_1 \times R^3$  roadmap has been recently reviewed in Ref. [35], focusing specially on the SU(2) gauge group like in our case. We address the reader to this review for an updated list of references. However, explicit mention is necessary for some recent papers that have considered and advocated a  $T_2 \times R^2$  strategy like the one addressed in this paper [36–38]. This might turn out to be a good way to put together the two different semiclassical strategies described in this introduction.

The paper is organized as follows. In the next section (Sec. 2) we start by making a short review of the semiclassical approach. This is then applied to our specific  $T_2 \times R^2$  geometry and boundary conditions. This shows the relevance of some particular fractional instanton solutions, some of whose properties are analysed. In Sections 2.3 to 2.5 we explain how for small torus sizes a picture of a dilute gas emerges, whose building blocks are the afore-mentioned fractional instantons. Qualitative and quantitative predictions are derived from this picture. In particular, in Section 2.6, we specify the semiclassical predictions on the density of the gas both on the lattice and in the continuum.

The next sections are devoted to presenting our results based on Monte-Carlo simulations of the SU(2) Yang-Mills theory, in order to test the predictions of the previous one. A partial collection of results was presented in a recent publication [39]. In Section 3.1 we describe the procedure followed in the generation and analysis of our numerical data. We explain in detail our simulation method, the smoothing/filtering methods applied, and the identification of structures and fitting of parameters. In this study, we have mainly focused on SU(2) Yang-Mills theory, but some small tests and comments are included about the extension to SU(N). Only some qualitative pictures considering general distributions of fluctuations and peaks are shown for the discussions of the methods in this Section.

Our main numerical results and analysis are presented in Section 4. The primary goal is an investigation for small torus sizes since it provides a clean and controlled setup for the semiclassical approach. It is shown how the numerical data matches with the predictions from the semiclassical analysis of an effective two dimensional gas of fractional instantons and anti-instantons, measuring some of the unknown parameters. All observables are

analysed, with particular attention being paid to the string tension and its relation with the density of the gas.

Although our main goal has been the study of the small torus sizes, for which the semiclassical predictions are supposed to hold better, in Section 5 we show some results concerning larger torus sizes. Our analysis allows us to determine the necessary modifications of our techniques in order to investigate the approach towards the limit of large torus sizes, in which we recover the full isotropic four-dimensional Yang-Mills theory.

In the last Section 6 we give a brief review of our results, and conclude with final discussions of the general picture and possible extensions of our work. We collect in appendices some interesting aspects that complement our work.

## 2 The semiclassical regime on $T_2 \times R^2$

### 2.1 Generalities about the semiclassical approximation

In this section we will focus on the semiclassical regime for which analytic predictions can be obtained and tested against our numerical results. This occurs when the size of the small torus is small enough so that the effective coupling is also small. Perturbation theory becomes a good approximation for short distance observables. However, certain properties of the theory are zero to all orders of perturbation theory and that is where semiclassical methods play a role. That is a well-known technique which has been essential to understand the properties of many field theories. Classical quantum field theory text-books like [40] dedicate a good deal of space to it. The method is a generalization of the well-known saddle point approximation for integrals over the complex plane. Recently, the field has been gaining focus and stronger versions, under the label *resurgence*, have been studied in certain examples of quantum systems and field theories (see Refs. [41–43] for a review).

A simple description of the idea implies that the path-integral is split into a sum of terms labelled by extrema of the action (classical configurations)  $A_\mu = A_\mu^{\text{clas}}$  which include small quantum fluctuations around them  $A_\mu = A_\mu^{\text{clas}} + A_\mu^{\text{quant}}$ :

$$Z \sim \sum_{A_\mu^{\text{clas}}} \int dA_\mu^{\text{quant}} e^{-\frac{1}{g^2} S(A_\mu^{\text{clas}} + A_\mu^{\text{quant}})}, \quad (2.1)$$

This is particularly relevant when computing observables for which the splitting is not terribly sensitive to the quantum part provided it is small:

$$O(A_\mu^{\text{clas}} + A_\mu^{\text{quant}}) = O(A_\mu^{\text{clas}}) + \mathcal{O}(g^2), \quad (2.2)$$

On the other hand the action can also be expanded for small quantum fluctuations

$$\frac{1}{g^2} S(A_\mu^{\text{clas}} + A_\mu^{\text{quant}}) = \frac{1}{g^2} S(A_\mu^{\text{clas}}) + \frac{1}{g^2} S^{(2)}(A_\mu^{\text{clas}}, A_\mu^{\text{quant}}) + \dots \quad (2.3)$$

The leading correction  $S^{(2)}$  is quadratic in the quantum fluctuations since the classical part is an extremum of the action. This quadratic piece can be dealt with by a rescaling the quantum fields  $A_\mu^{\text{quant}} = gQ_\mu$  and performing a Gaussian integration over  $Q_\mu$ . The

Jacobian of the transformation induces a factor  $g$  for each degree of freedom, and the Gaussian integration over  $Q$  a factor which we write as

$$e^{-S_Q(A_\mu^{\text{clas}})}, \quad (2.4)$$

Altogether we have

$$Z \sim \sum_{A_\mu^{\text{clas}}} e^{-\Gamma(A_\mu^{\text{clas}})} g^{\text{nqdf}} + \text{higher orders in } g, \quad (2.5)$$

where the free energy of each configuration is

$$\Gamma(A_\mu^{\text{clas}}) = \frac{1}{g^2} S(A_\mu^{\text{clas}}) + S_Q(A_\mu^{\text{clas}}) \quad (2.6)$$

The factor  $g^{\text{nqdf}}$  is irrelevant if the number of quantum degrees of freedom (nqdf) is the same for all classical fields. However, there are certain directions for which the second order term  $S^{(2)}$  vanishes. These are the zero-modes, and in practice imply a weight  $g^{-\text{nzm}}$  in terms of the number of zero-modes (nzm) of each classical field. As a matter of fact, the  $S^{(2)}$  is given by a quadratic form involving the Dirac operator in the adjoint representation. Hence, the number of zero modes can be obtained from the index theorem.

Our presentation has been quite schematic. For example, the fact that there are infinitely many classical fields turns our symbolic sums into integrals. For certain families of classical solutions these integrals range over collective coordinates labelling the ensemble. Other important questions that have been ignored are gauge fixing, ghosts, and the presence of ultraviolet divergences. We point the reader to the beautiful paper by 't Hooft [44] where all the technical issues are addressed in computing the quantum fluctuations around the BPST instanton solutions.

The semiclassical approach also applies on the lattice. Even more so, since in this case the path integral reduces to an integral over real variables and many of the divergences are absent. On a finite volume also the number of degrees of freedom becomes finite. However, even in this case unexpected difficulties might appear as seen in papers as [15, 16] for which the space of classical solutions (torons) becomes an orbifold and the collective coordinate formalism breaks down. One of the advantages of using twisted boundary conditions is that it eliminates some of these difficulties[45, 46].

## 2.2 Classical solutions

After this rather general presentation, let us apply it to the case at hand. We have to look for solutions of the euclidean classical equations of motion. It is in this context that the BPST instanton solution was found [47]. However, contrary to what many people think, this is not the only basic solution and not even the most relevant for our study. We are looking at solutions on the torus of the Yang-Mills euclidean equations of motion. As mentioned earlier, 't Hooft put forward that the topology is not only given by the instanton number  $Q$ , but also by certain  $Z_N$  fluxes traversing the planes of the torus. If these fluxes are present, we say that we have twisted boundary conditions. In our study

we are considering a small 2-torus with non-zero flux  $(-1)$ . Although we are considering the range of the remaining 2 directions as infinite, we might as well consider that they are compactified in a very large torus. This is a practical option which is typically adopted in lattice gauge theory studies. The physics of the theory is not affected by the choice of boundary conditions in this big 2-torus. However, it affects the classical solutions and this can be used as a tool as we will see. If we put also a non-zero flux in this large torus, then the topological charge becomes fractional  $Q = n + 1/2$ . Bogomolny bound implies that the minimal action configuration would be non-trivial and self-dual, we call such a configuration a fractional instanton. This problem was studied in Ref. [48], where it was found that the basic  $Q = 1/2$  solution has an action density which peaks at a certain point (its center) and tends to zero action density as we move away from its center in the large torus. Furthermore, if one scales all coordinates by the torus size  $l_s$  the solution converges to a fixed limit as the size of the big torus goes to infinity. It is this limiting solution what we call a  $T_2 \times R^2$  fractional instanton. Because of its properties it was also referred as a vortex-like fractional instanton. The properties of the solution (as described in Ref. [48]) are the following:

1. To the level of precision of the action minimization method (at the permille level) the configuration is self-dual.
2. The action density and all gauge invariant observables are functions of the coordinates  $x_\mu/l_s$ , where  $l_s$  is the size of the small torus.
3. The action density has a peak at a given location (its center) and has circular invariance under rotations in the big plane around this point.
4. Furthermore, the action density decreases as one moves away from this point in the radial direction  $r/l_s$ , and in an exponential manner for large enough distances.
5. The value of the Wilson loop in the large plane and centered at the instanton position tends to  $-1$  as the size of the loop grows. This implies that the instanton behaves like a center-vortex perpendicular to the big plane.
6. From self-duality and the Bogomolny bound [49, 50] one concludes that the action is half that of an instanton ( $4\pi^2/g^2$ ).
7. The solution is certainly non-unique because its center breaks translational invariance. However, these are the only continuous degrees of freedom. This follows from the index theorem implying that the space of solutions depends on only 4 parameters ( $4QN$  for our  $N = 2$   $Q = 1/2$  case).
8. Computing the Polyakov loops in the two small torus directions at the center of the solution we find  $P_1 = \pm 1$  and  $P_2 = \pm 1$ .  $(Z(2))^2$  center symmetry maps the 4 different solutions onto each other.

Given the previous properties, one can compute the weight associated with every fractional instanton (See Eqs. (2.5)(2.6)) . Given the number of zero modes and the value

of the action we conclude that when going from the instanton to the fractional instanton contribution one gets

$$\frac{1}{g^8} e^{-8\pi^2/g^2 - S_{QI}} \longrightarrow \frac{1}{g^4} e^{-4\pi^2/g^2 - S_{QF}}. \quad (2.7)$$

The quantum contribution to the free energy for the instanton  $S_{QI}$  has been computed by 't Hooft [44]. Unfortunately, the corresponding quantity for the fractional instanton ( $S_{QF}$ ) is not known, but our work provides a numerical estimate of its value.

Obtaining a precise numerical approximation to the  $Q = 1/2$  fractional instanton can be done as in Ref. [48]. A more recent and complete analysis of the solution will be presented elsewhere [51], but for the purpose of this paper we have used various numerical approximations using  $L_t^2 \times L_s^2$  lattices of various sizes. The lattice size in the short torus directions acts as a lattice spacing error  $a = 1/L_s$ . Typical errors in the approximation are given in powers of  $a$ . The size of the errors depends on the lattice quantity that is being used. For example, the value of the Wilson action  $S_W$  can be measured after minimizing its value, we get

$$\frac{4}{\beta} S_W(L_s) = 4\pi^2(0.9999(7) - 0.44(5)/L_s^2). \quad (2.8)$$

Notice that on the lattice this is the quantity that enters the semiclassical weight factor. Computing now the clover defined lattice action  $S_C$ , we see that it can be fitted to the formula:

$$g^2 S_C(L_s) = 4\pi^2(1.00027(21) - 2.417(22)/L_s^2). \quad (2.9)$$

The lattice approximation to the total topological charge  $Q_L$  gives

$$Q_L = \frac{1}{2}(1.00006(3) - 2.441(3)/L_s^2). \quad (2.10)$$

We see that both formulas extrapolate to the expected self-dual values with less than permille errors. No significant dependence is seen on the large torus lattice size. The maximum topological charge density for a single fractional instanton is obtained as<sup>1</sup>

$$Q_{\max} = 2.274(7) - 7.0(8)/L_s^2. \quad (2.11)$$

For the purposes of this paper we will now focus on the 2-dimensional action density obtained after integrating over the two short directions  $S_2(x, y)$ . On the lattice one measures the sum of the corresponding plaquettes which is given by  $S_2(x, y)/L_s^2$ . This observable will be useful later to identify the fractional instantons present in the Monte Carlo configurations. In Fig. 1 we show the distribution of this observable in 4 different projections. As an example we take the  $11^2 \times 45^2$  configuration. Fig. 1a displays  $S_2(n_1, n_2)/11^2$  as a function of the lattice coordinates of the large plane for this configuration as a 3D plot. The corresponding contour plot is given in Fig. 1b, in which one notices the approximate

---

<sup>1</sup>When comparing to the lattice results, the value has to be divided by  $L_s^4$ .

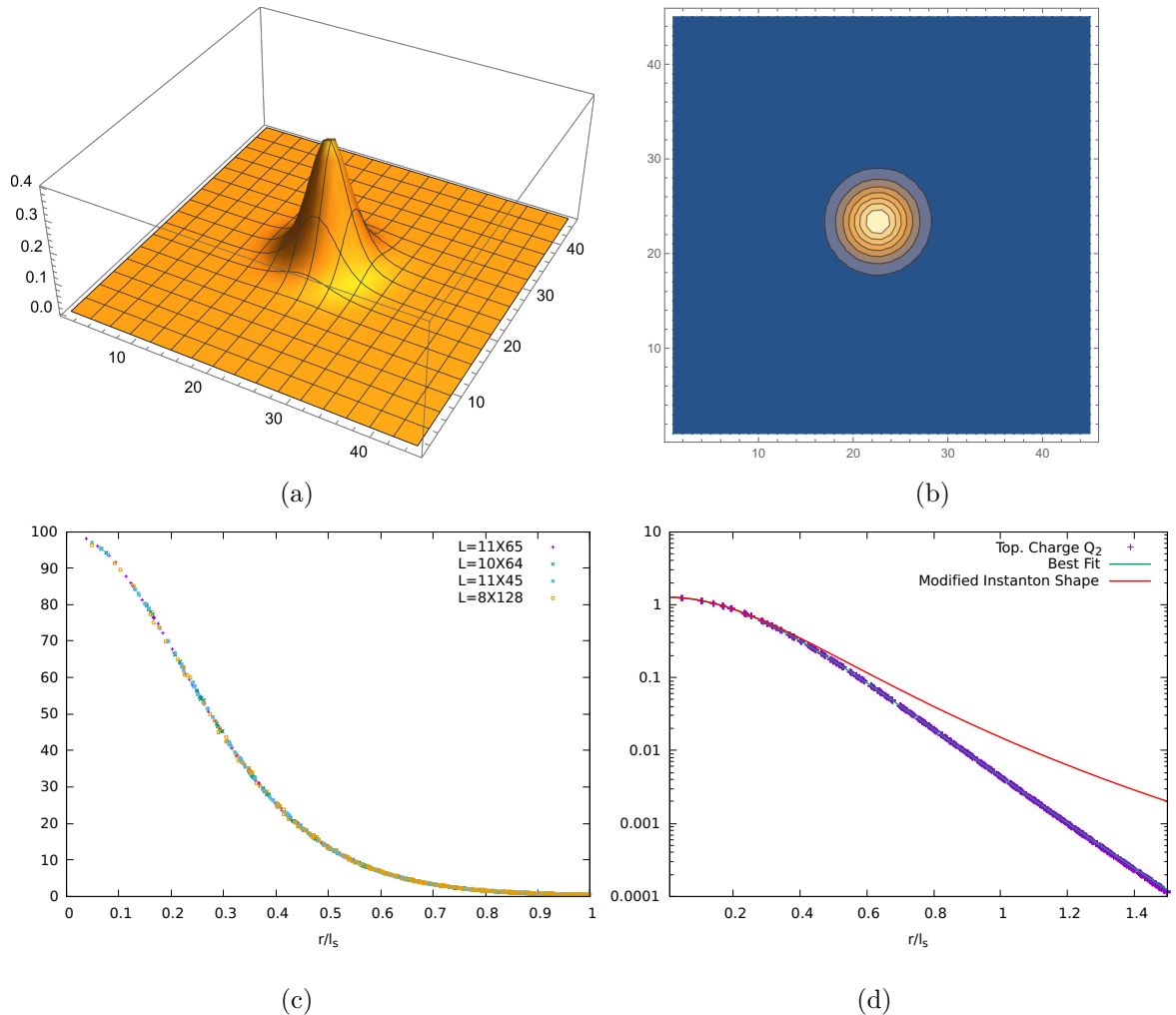


**Figure 1.** This figure shows several projections of the  $SU(2)$  vortex-like fractional instanton. a) Integrated energy density profile  $S_2(n_1, n_2)$  in lattice units for a  $11^2 \times 45^2$  approximation; b) the corresponding contour plot; c) The integrated profile  $S_2(r/l_s)$  as a function of distance to center  $r$  for various numerical approximations; d) Topological charge density in logarithmic scale compared with fitting functions (see text).

circular symmetry of the solution around its central peak. This symmetry and the universality of the solution is more precisely appreciated in Fig. 1c. This shows the radial profile of the observable  $S_2(r \cos(\theta), r \sin(\theta))$  obtained from different lattice approximations. Any lattice correction as well as possible violations of circular symmetry (i.e.  $\theta$  dependence) show up as small fluctuations around a universal curve. In logarithmic scale one easily sees that for large sizes the curve decays exponentially (Fig. 1d).

An interesting observable is the value  $S_2$  at the maximum.<sup>2</sup> Our lattice approximations

<sup>2</sup>We use in this case a simple quadratic interpolation of the form  $A - B_1(x - x_0)^2 - B_2(y - y_0)^2$  to get the approximate peak height and position.

can be fitted to the formula

$$S_{2,\max} = 100.27(20) - 283(20)/L_s^2. \quad (2.12)$$

The maximum of the integrated topological charge density follows just from self-duality (1.270(3)). Notice that the extrapolated peak value is not far from  $32\pi$ , which is the same value obtained for a 2D projection of an instanton of size  $\rho = l_s/\sqrt{2}$ . However, the shape of the function does not agree with that of an instanton since it decays exponentially with  $r$  and the total integral is  $4\pi^2$  instead of  $8\pi^2$ . Even in the neighbourhood of the center, the shape of the topological charge density differs from the corresponding one of BPST instantons. This is interesting since it can be used to distinguish fractional instantons. A simple function that fits the topological charge density 2D profiles  $q(x)$  for  $r \leq 0.2$  is given by  $q(x) = q_{\max}(1 + r^2/\rho^2)^{-3}$ . Extrapolating to the continuum limit our numerical results we obtain  $q_{\max} = 1.276(5)$  and  $\rho^2 = 0.297(10)$ . Notice that the combination  $Q_I = \pi\rho^2 q_{\max} = 0.595(5)$ , which differs considerably from the value 1 valid for BPST instantons.

The previous fit only matches the profile for  $r \leq 0.2$ . This is particularly clear when comparing the logarithm of the topological charge density with the modified instanton shape  $q(x)$  displayed in Fig. 1d. A good fit to the action density shape covering the full range can be obtained by approximating the logarithm of the function by a rational function of the form:

$$\log(S_2(r)/S_2(0)) = -\frac{Br^2 + F \cdot Dr^3}{1.0 + Cr + Dr^2} \quad (2.13)$$

For our  $11^2 \times 45^2$  approximation the best fit parameters are  $B = 9.73$ ,  $C = 0.63$ ,  $D = 1.30$  and  $F = 5.2$ . The comparison is shown in Fig. 1d, where the integrated topological density is plotted together with the best global fit described above. We see that the two functions describe well the data for  $r/l_s \leq 0.2$  but differ considerably at large distances, given the strong exponential fall-off (obvious given the large value of  $F$ ). As a matter of fact, using the same function for the full range introduces distortions in the parameter values. A better way to describe the function is to use different fits in different regions. Concerning the exponential tail we found that for  $r > 1$  the  $S_2(r)$  can be described at the 5% level by  $170(8) e^{-2\pi r}/r$ .

### 2.3 Description of the semiclassical components

Our results so far have considered only isolated fractional instanton (FI) solutions corresponding to the minimum action with twisted boundary condition in the big and small torus. The solution can be translated in space, which implies an entropy factor that scales with the area of the large torus. This overcomes the price, in terms of probability, of adding more FIs. Thus, one has to consider also multi-fractional instantons in our semiclassical description. Consequently, as expected from thermodynamic principles, the total action diverges in the infinite volume limit. However, as we will see in the next section, the probability per unit area of containing one FI is small when the small torus size  $l_s$  is small. On the lattice this probability depends both on  $L_s$  and  $\beta$ . At these small densities

the separation is much larger than the size of the objects and the most probable configurations amount to a dilute gas of FI. In this situation, the total free energy for one of these configurations becomes very approximately the sum of the free energies of each FI. Indeed, even at closer distances the action of such a multi-FI configurations is exactly additive as it follows from the index theorem and the Bogomolny bound.

However, the same arguments given above imply that one should also include fractional anti-instantons (AFI). At these large separations the interaction energies are very small, and the free energy of a typical configuration having both FI and AFI would be very approximately the sum of all its components. Notice, however, that these configurations containing both FI and AFI will no longer be classical solutions. There is no topological protection, and hence it is expected that a FI-AFI pair can be continuously connected to the configuration with both absent, having smaller action. However, the directions of instability are probably very few and the slopes are small for large separations, so they are amply compensated by quantum fluctuations. These expectations are verified by the study of the behaviour under cooling and gradient flow (see for example in a previous paper [52]): the FI-AFI pair is eventually annihilated by the flow, but this happens at large times (gradient flow time, steps of cooling) when the separation is large compared to the size of the objects.

In summary, in the semiclassical description, the "classical" configurations are given by a gas composed of both FI and AFI at random locations. At low densities, expected for sufficiently small  $l_s$ , the gas is dilute and the free energy is the sum of that of its constituents. We recall that the objects occupy the full small 2-torus, and most of its properties depend very slightly upon the location of the center within it. Thus, effectively one can say that one is dealing with a two-dimensional gas.

## 2.4 Properties of the 2D gas of FI and AFI

In the dilute situation, the probability of having one object per unit area is a small number, which should be proportional to the path-integral weight of such an object. The same value applies to FI and to AFI. This together with the randomness of 2D location tells us that the distribution of the gas is Poissonian. To do calculations it is sometimes better to take the distribution to be multinomial, which converges to Poisson in the dilute situation. The multinomial can be thought as a way to take into account the finite size of the objects. We will explain this below.

Let us compute the probability for a given configuration having  $n_+$  FI and  $n_-$  AFI as follows. Let us take a portion of the plane of area  $A$  and divide it into a large number  $M$  of small portions of the same size with area  $A_0$  (thus  $A = MA_0$ ). The portions are large enough to contain a FI fully but small enough so that the probability of having two objects in each portion is negligible. In each portion of size  $A_0$  the probability of having one FI is  $p_0$ , the probability of having one AFI is also  $p_0$  and the probability of having nothing is  $1 - 2p_0$ . Notice that we can write  $p_0 = \bar{p}A_0$ , where  $\bar{p}$  is the probability per unit area. Then, the probability that the big area contains  $n_+$  FI and  $n_-$  AFI is given by the multinomial

distribution:

$$P(n_+, n_-) = \frac{M!}{n_+!n_-!(M - n_+ - n_-)!} p_0^{(n_+ + n_-)} (1 - 2p_0)^{M - n_+ - n_-}. \quad (2.14)$$

Notice that the sum over all possible values of  $n_{\pm}$  is 1. The Poisson distribution is obtained when taking the limit  $M$  large,  $p_0$  small with the product  $p_0 M$  fixed:

$$P(n_+, n_-) \longrightarrow P'(n_+, n_-) = \frac{(p_0 M)^{n_+ + n_-}}{n_+!n_-!} e^{-2p_0 M}. \quad (2.15)$$

From these distributions one can easily calculate all the moments. For that purpose we can replace the probabilities by variables  $x_{\pm}$  for one FI/AFI and  $1 - 2x_0$  for no object. Summing up one gets a generating function

$$Z(x_+, x_-, x_0) = (1 - 2x_0 + x_+ + x_-)^M, \quad (2.16)$$

from which all moments can be obtained by differentiation at  $x_+ = x_- = x_0 = p_0$ . For example, the mean number of fractional instantons is given by

$$\langle n_+ \rangle = \langle n_- \rangle = p_0 M = \bar{p} A. \quad (2.17)$$

Notice that this mean number is precisely the quantity appearing in the Poisson distribution. From the previous expression one sees that the 2D density of objects becomes

$$\rho_{2D} = \frac{1}{A} \langle (n_+ + n_-) \rangle = 2\bar{p}. \quad (2.18)$$

If each object has topological charge  $Q = \pm 1/2$  one can also compute the distribution of topological charge. The mean value is zero but the dispersion (i.e. the 2D topological susceptibility) becomes

$$\hat{\chi}_{2D} = \frac{1}{4A} \langle (n_+ - n_-)^2 \rangle = \frac{2Mp_0}{4A} = \bar{p}/2, \quad (2.19)$$

which is equal to the density divided by 4. Higher order moments can be easily computed. Later on we will give the full distribution.

Finally, we notice that since the fractional instantons behave as  $Z_2$  vortices, one can evaluate the expectation value of a Wilson loop  $W$  covering the full area  $A$  by simply summing up the contribution of each object:

$$\langle W \rangle = \langle (-1)^{(n_+ + n_-)} \rangle = (1 - 4p_0)^M. \quad (2.20)$$

This shows that the expectation value for these large loops decays with the area and the string tension is given by

$$\sigma = -\log(1 - 4p_0)/A_0 \sim 4p_0/A_0 = 4\bar{p} = 2\rho_{2D}. \quad (2.21)$$

The last result is precisely the result obtained for the Poisson distribution, and can be labelled *thin abelian vortex approximation* (TAVA). The non-abelian character of the FI

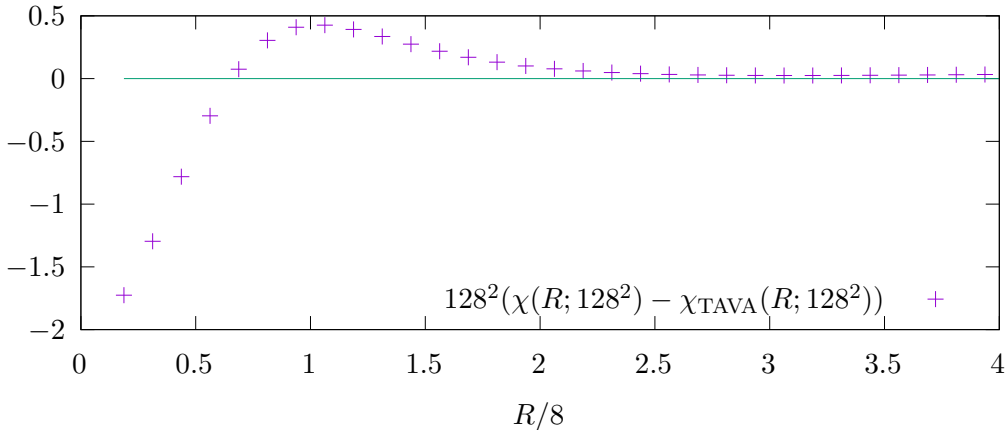


**Figure 2.** Square Creutz ratios  $\chi(R)$  averaged over the plane obtained for a numerical approximation to the SU(2) fractional instanton on a  $8^2 \times 128^2$  lattice after subtracting the same quantity for the thin abelian vortex approximation (TAVA) computed on a torus of size  $A = 128^2$  and multiplying by the lattice area of the big torus ( $128^2$ ).

and their finite size can correct this slightly, but this should be very approximately correct in the dilute situation. Indeed, it is possible to test this with our numerical FI configurations. For practical purposes it is useful to consider square Creutz  $\chi(R)$  ratios as a good way to estimate the string tension since they get rid of perimeter contributions. Given  $W(R, T)$  Wilson loops of  $R \times T$  rectangular shape, the ratios are defined as

$$\chi(R) \equiv -\log \left( \frac{\langle W(R, R) \rangle \langle W(R-1, R-1) \rangle}{\langle W(R, R-1) \rangle \langle W(R-1, R) \rangle} \right) \quad (2.22)$$

Now suppose we have a big torus of area  $A$  containing a single fractional instanton. Using our previous analytic computation of Wilson loop expectation values, one can compute the corresponding square Creutz ratios  $\chi(R; A)$  (averaged). This is just the exact value for the 2-dimensional  $Z_2$  gauge theory. For large area  $A$ , the result tends to  $2/A$  which is equal to twice the density. However, there are sizeable differences when  $R^2$  becomes comparable with  $A$ . We compared this result with the computation of square Creutz ratios for an  $8^2 \times 128^2$  lattice containing a single fractional instanton. The area in this case is  $A = 128^2$  and the density  $2/A$ . In Fig. 2 we show the difference between our measured Creutz ratios minus the result of the thin abelian vortex approximation. Notice that the results agrees for large values of  $R$ . However, our vortex has a size of order  $L_s = 8$  and Creutz ratios for  $R/L_s$  smaller than 1 show a strong size dependence. Curiously at  $R = L_s$  the Creutz ratio divided by the density peaks and becomes 2.4 instead of 2. It is important to keep this in mind when interpreting our Monte Carlo data.

In summary, as it is well known, our FI-AFI vortex gas is expected to confine with string tension which is approximately 2 times the density. Furthermore, With our formulas, higher order moments of the density or topological charge distribution can be computed easily for both the multinomial and the Poisson distribution.

## 2.5 Role of twist and of ordinary $Q = 1$ instantons

In this section we will comment on certain slight modifications to what we have just described. We argued, that to have a fractional topological charge object, one must have a non-zero twist both in the small torus as well as in the big torus. The twist in the small torus is crucial in our study as long as its size is small in terms of the inverse Lambda parameter of the theory. However, at large sizes, boundary conditions should not matter and the results must coincide with those that are obtained using periodic boundary conditions. We have actually verified this by computing the string tension at sufficiently large lattices with and without twist. The results agreed within errors.

The effect of putting a zero or non-zero twist in the big plane can be understood if one realizes that twist is just a flux modulo  $N = 2$ . Thus, even if we do not have twist in the large plane, one will still produce fractional instantons, but always an even number of them. This certainly affects the distributions and calculations that we did in the previous section. If we put a twist in the big plane, the total number of objects  $n_+ + n_-$  has to be odd, and if we don't, it has to be even. Most of our simulations are done in this second case. Computing expectation values in the modified distribution is fairly easy by simply excluding the odd numbers:

$$\langle O \rangle_{\text{mod}} = \frac{\langle O(1 + (-1)^{(n_+ + n_-)}) \rangle}{\langle (1 + (-1)^{(n_+ + n_-)}) \rangle}, \quad (2.23)$$

where the right-hand side contains expectation values with respect to the unconstrained distribution of the previous subsection. Thus, one gets for example

$$\langle n_+ \rangle_{\text{mod}} = Mp_0 \frac{1 - (1 - 4p_0)^{M-1}}{1 + (1 - 4p_0)^M} = \langle n_+ \rangle \frac{(1 - e^{-4\langle n_+ \rangle})}{(1 + e^{-4\langle n_+ \rangle})}. \quad (2.24)$$

Clearly the correction is negligible when the mean number of objects is not very small.

For future purposes, let us evaluate explicitly the distribution of topological charge. That is equivalent to the distribution of the quantity  $(n_+ - n_-)/2 = Q$ . This distribution can be easily obtained for the constrained Poisson probability distribution using  $n_+ = n_- + 2Q$

$$P(Q) = \frac{1}{\cosh(2p)} \sum_{n_-} \frac{p^{(2Q+2n_-)}}{n_-!(2Q+n_-)!} = \frac{I_{2Q}(2p)}{\cosh(2p)}, \quad (2.25)$$

where  $I_n(x)$  is the modified Bessel function and  $p = p_0M = \bar{p}A$ .

Another distribution which turns out to be useful in interpreting our data is the distribution of minimum distance from an object to the closest one. Given a configuration with area  $A$  having  $n_+$  fractional instantons and choosing one of them, the remaining  $n_+ - 1$  have a probability  $1 - \pi d^2/A$  of being at a larger distance than  $d$  from our selected FI. Then the probability that all of them are outside a circle of radius  $d$  from our FI is

$$(1 - \pi d^2/A)^{n_+ - 1}. \quad (2.26)$$

Convoluting this probability with the one of having  $n_+$  fractionals we get

$$P(d) \propto e^{-p} \sum_{n_+} \frac{(p(1 - \pi d^2/A))^{n_+}}{n_+!} = e^{-\pi p d^2/A}. \quad (2.27)$$

where  $p = \langle n_+ \rangle$ . This combines with a prefactor  $d$  (coming from changing measure from area to length) to give a Maxwellian type of curve. Our derivation assumes that the fractional instanton have zero width and can be put together with other at arbitrarily short distances. Thus, we expect that at long distances the shape is correct but might get corrections for small values of  $d$ . Notice that from the previous distribution one can deduce that the distribution has a peak at  $d_{\text{peak}} = 1/\sqrt{\pi\rho_{2D}} = \sqrt{A}/\sqrt{2\pi\langle n_+ \rangle}$  and a mean value  $\bar{d} = \sqrt{\pi/2} d_{\text{peak}}$ .

In relation to this, an aspect to be addressed is whether ordinary instantons and anti-instantons of  $Q = 1$  are also present. The answer is certainly yes. However, the probability to create an instanton goes like the square of that of a fractional instanton and if this probability is small one expects many less instantons. Notice, however, that instantons do not contribute to the string tension but contribute to the topological susceptibility. To generate a non-zero string tension it is crucial that the fractional instantons are independent. If all FI appear in fixed size molecules made of pairs of them, the string tension would also vanish.

## 2.6 Scaling of the densities and the continuum limit

As explained in the previous section, the semiclassical approximation can be studied both in the continuum and on the lattice. In this section we will see how the two are connected. Let us consider 4d lattice of size  $L_s^2 \times L_r^2$  where  $L_r \gg L_s$  and SU(2) lattice Yang-Mills theory is generated with Wilson action and coupling  $\beta$ . Now consider a dimensionless quantity which we call diluteness  $D$  as follows:

$$D = L_s^2 \rho_{2D}^L = \frac{L_s^2}{L_r^2} \langle (n_+ + n_-) \rangle, \quad (2.28)$$

where  $\rho_{2D}^L$  is the 2D density computed by dividing the number of objects by the area of the large torus. The big area is large, so the diluteness can only depend on  $L_s$  and  $\beta$ . The diluteness must be proportional to the probability to create a fractional instanton per unit area so according to our discussion in Sec. 2.2 we expect

$$D = A(L_s) \beta^2 e^{-\pi^2 \beta}. \quad (2.29)$$

An equivalent calculation in the continuum gives a diluteness that depends on  $l_s$  and the coupling  $g$ . But as it is well-known, the coupling has to be defined in a scheme and that introduces a dependence on an energy scale  $\mu$ . Because of dimensional reasons, the diluteness can only depend on  $\mu l_s$  and  $g(\mu)$ . However,  $\mu$  is an arbitrary scale and the dependence on  $\mu$  and  $g(\mu)$  can be eliminated in terms of a new scale: the Lambda parameter  $\Lambda$ . Thus, at the end of the day, the diluteness would be a function of  $l_s \Lambda$ , which is the only dimensionless combination. A similar thing happens on the lattice where the

scale is the lattice spacing  $a$  and combined with the lattice coupling  $\beta$  they should be traded by the Lambda parameter. This can be done using the beta function of the theory. We can write

$$a\Lambda_L = \exp\left\{-\frac{3}{11}\pi^2\beta\right\} \left(\frac{6\pi^2}{11}\beta\right)^{51/121} \quad (2.30)$$

Using this formula we can rewrite the expression of the diluteness as follows

$$D = A(l_s/a)(a\Lambda_L)^{11/3} \left(\frac{11}{6\pi^2}\right)^{11/17} \beta^{5/11} \quad (2.31)$$

In the continuum limit this should only depend on  $l_s\Lambda_L$  and this implies that, up to logarithmic corrections, the prefactor behaves as

$$A(L_s) \sim A_0 L_s^{11/3} \quad (2.32)$$

This implies that in the continuum the diluteness goes as  $(l_s\Lambda)^{11/3}$  and the 2D density as  $(l_s\Lambda)^{5/3}$ . This is the result that one obtains in a continuum calculation by replacing  $g(\mu)$  in the naive formula by  $g(l_s)$ .

### 3 Ensemble generation and numerical analysis

The ultimate aim of this work is to identify the relevance of different semiclassical contributions in the Yang-Mills vacuum and their role in inducing the fundamental mechanisms of the theory, like confinement. This can be achieved by the analysis of the configurations generated by Monte Carlo simulations. The semiclassical approximation is expected to work well for small values of  $l_s$ . As explained in previous sections, in this regime the system can be described as a two-dimensional dilute gas of fractional instantons. Our first goal will be to verify the theoretical predictions by the analysis of our configurations and develop the most appropriate methods. We will then monitor the evolution of the system as we gradually increase the size of the two torus. Extending the analysis, we aim at investigating the evolution of the topological structures as we move from the semiclassical regime towards the infinite volume limit. This means we want to study the Yang-Mills vacuum as a function of  $l_s$  and identify semiclassical contributions for a large set of ensembles. In our simulations we consider mainly SU(2) Yang-Mills theory; only some outlook on SU(3) and SU(4) is presented in the Appendix. Some details of the simulation methods are explained in Sec. 3.1.

Identification of semiclassical structures has been applied in several previous studies. Most of them were focused on instantons, but also related to fractional instantons as they appear in a  $T_3 \times R$  setting. The procedure consists of three steps: the first is a filtering of the ultraviolet noise from the configurations, as explained in Sec. 3.2. The second step is the fitting of structures, see Sec. 3.3. In a third step, as detailed in Sec. 3.5, the fit parameters are related to certain semiclassical objects like instantons based in the behavior of the distributions discussed in Sec. 3.4.

$\beta$	$a$ (fermi)	$t_{gf}$			
2.4	0.11630	3.52			
2.45	0.985	5.34			
2.5	0.08194	7.34			
2.55	0.07089	10.87			
2.6	0.05938	15	$L_s$	$L_r$	$\tau = \sqrt{8t_{gf}} a$
2.65	0.05072	20.39	4-14	64, 104	twist
2.7	0.04337	27.37			$(2,3), \vec{k} = 0, \vec{m} = (1, 0, 0)$
2.75	0.03745	36.37			
2.8	0.03238	47.84			

**Table 1.** LEFT: List of lattice couplings used, together with the corresponding lattice spacing values and lattice gradient flow times applied (further details in the Appendix Tab.2) RIGHT: List of Lattice sizes simulated, twist employed and approximate smearing radius in physical units. (Fermi unit  $\equiv \sqrt{5}/\sqrt{\sigma}$ )

### 3.1 Monte Carlo simulations

The Monte Carlo simulations are performed on a lattice of size  $L_s^2 \times L_r^2$  with  $L_r \gg L_s$ . Periodic boundary conditions are applied in the large  $R^2$  directions (each with  $L_r$  lattice points), while twisted boundary conditions are applied in the short  $T_2$  directions, having  $L_s$  lattice points. The physical size of the  $T_2$  directions is  $l_s = a(\beta)L_s$ , where  $a(\beta)$  is the lattice spacing at a given coupling. All ensembles presented in this work are generated with a plain Wilson gauge action. The scaling of the lattice spacing has already been determined in several previous studies.<sup>3</sup> The full list of lattice sizes,  $\beta$  values and the corresponding physical sizes  $l_s$  are given in Tab. 1 and 2. Details about the implementation of twisted boundary conditions have already been explained in several publications [19, 54, 55]. We have used a standard hybrid Monte-Carlo and a heat-bath algorithm to generate the configurations.

We have carefully monitored fluctuations of the topological charge in our simulations. This is essential to ensure thermalization and proper sampling. We have tested that both hot (random) and cold (zero-action) initial boundary conditions lead to compatible results and measured the autocorrelation time of the topological charge. This limits our simulations to the parameter range of  $\beta \leq 2.7$  since substantial topological freezing is observed at larger  $\beta$ .

The generated ensembles allow for a direct measurement of observables such as the expectation values of Wilson loops, Polyakov loops, topological charge, etc. In Fig. 3 we show the string tension to illustrate the basic effect of the finite size  $l_s$ . As expected, the string tension becomes smaller towards the semiclassical regime. However, the interpolation to infinite volume seems smooth and continuous. Our main analysis requires in addition a filtering of short-distance (ultraviolet) noise from the gauge configurations in order to

<sup>3</sup>We have chosen [53] as a reference. The values are usually expressed in units of the inverse of the square root of the string tension and converted using a reference scale of  $\sigma = 5 \text{ fm}^{-2}$  for the string tension.

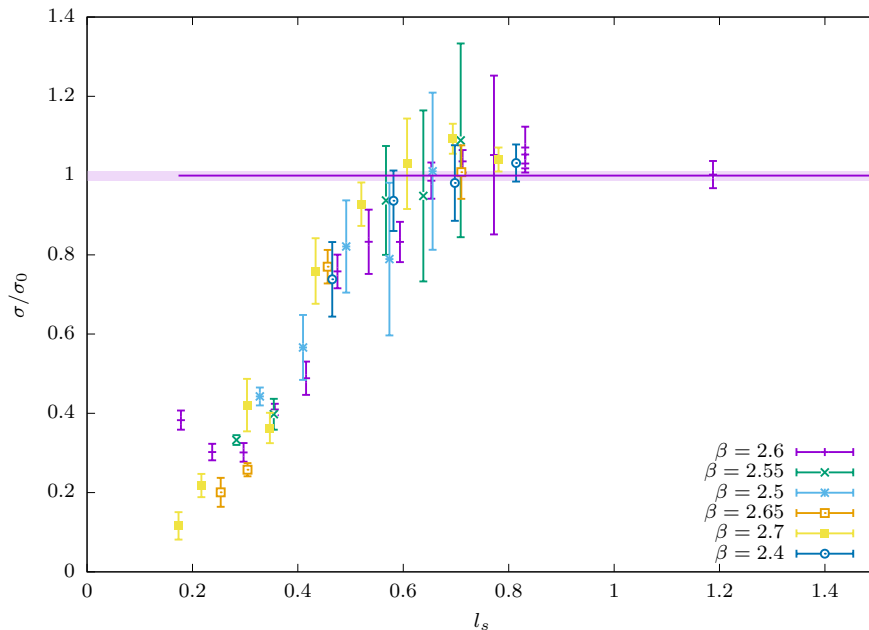


**Figure 3.** String tension  $\sigma$  as a function of  $l_s$  relative to the largest volume result  $\sigma_0$  in SU(2) Yang-Mills theory. The data are obtained from a two-step fit. In a first step the static quark anti-quark potential is obtained from the Wilson loops in  $R^2$  plane. The second step is a fit of the potential to  $V(r) = A/r + B + \sigma r$ . This result is obtained with APE smearing in directions orthogonal to  $R^2$ , but without gradient flow.

reveal semiclassical structures. We have used gradient flow for this purpose. The details of the filtering procedure are discussed in the next section.

### 3.2 Gauge noise filtering

It is well known that the lattice discretization of Yang-Mills theory does not provide a well-defined notion of topology in the presence of short-range fluctuations introducing lattice artefacts. Smoothing methods are required to remove these artefacts. Methods like cooling, gradient flow, or smearing correspond to a modification of the gauge configurations, while other methods like the adjoint zero-mode method [52, 56, 57] rely on modified observables that coincide with the standard ones in smooth backgrounds and decrease the effect of high-frequency noise. However, the methods based on zero modes are computationally more demanding. In this work, we have used the gradient flow [58] as a filtering method since we want to scan a large parameter range efficiently. It is an evolution of the gauge fields in a fictitious time  $t_{gf}$  towards saddle points of a gauge action. The effects are comparable to cooling [59]. We have applied standard integration techniques explained in these references. The choice of the lattice gauge action in the gradient flow, which is independent of the gauge action used in the simulations, leads to different flow types. The leading order contribution of these flow types is the same, but subleading parts introduce relevant differences distorting some topological structures. The gradient flow evolution leads to smearing over a length-scale  $\tau = \sqrt{8t_{gf}}$ , which can be called the smearing radius [60].

The gradient flow has several effects on the gauge ensemble and introduces an additional dependence on the parameter  $\tau$ . Different approaches can be used to resolve this dependence on the flow time. One can fix the flow time in lattice units and extrapolate to the continuum limit. This would correspond to a modification of the lattice discretization at the ultraviolet scale, which should leave the universal continuum limit unaffected. Alternatively one could try to identify an intermediate range of  $\tau$ , where lattice artefacts and ultraviolet noise are already removed, but the leading order in the flow time expansion around  $\tau = 0$  can still be determined. This is in particular useful for ultraviolet finite observables, which can be extrapolated to zero flow time. The third possibility is to keep  $\tau$  fixed in physical units and extrapolate the continuum limit. The dependence on the reference scale introduced in this way, can be monitored afterwards independent of the lattice regularization. For finite quantities, the scale can be removed in a second extrapolation step afterwards.

In our present work we consider first a fixed  $\tau$  in physical units in order to provide a clear picture of the topological structures and the semiclassical limit. Afterwards, we estimate effects of the flow in an investigation of the dependence on  $\tau$ . The relation between the density of topological structures and observables should hold for any flow time, while the density itself is slightly changed during the flow.

We also present and discuss some main effects of the gradient flow in the following sections. Some of these effects can be summarized as follows:

1. The fractional instantons in the semiclassical regime are very stable under the flow, even up to very large flow times.
2. A pair of fractional instanton and fractional anti-instanton with a sufficiently small distance between the two objects is annihilated during the gradient flow. This can be considered a physical effect related to the smoothing procedure and hence appears for any type of gradient flow. Similar effects occur for a pair of (BPST) instanton and anti-instanton.
3. Depending on the type of flow, instantons get deformed. This effect has been discussed in the context of cooling in [61], later also related to gradient flow in [62], with some recent verification in [63]. This phenomenon was studied in detail and explained in Ref. [64]. In the absence of twist this is due to the fact that self-dual solutions of  $Q = 1$  on the torus do not exist [65]. The action decreases with the torus size and only saturates the Bogomolny limit in the singular case of  $\rho = 0$ . On top of this, lattice artefacts also induce a dependence of the lattice action on the instanton size. Thus, Wilson flow also produces a decrease of the instanton size until it disappears. Fortunately, changing the lattice action the effect can be reversed and the instanton size can be made to increase even compensating the continuum phenomenon mentioned before. For this reason, this is called "overimproved" flow.

Typically, lattice artefact corrections are particularly relevant along the directions of the moduli space of the continuum solutions. However, for the  $Q = 1/N$  fractional instantons

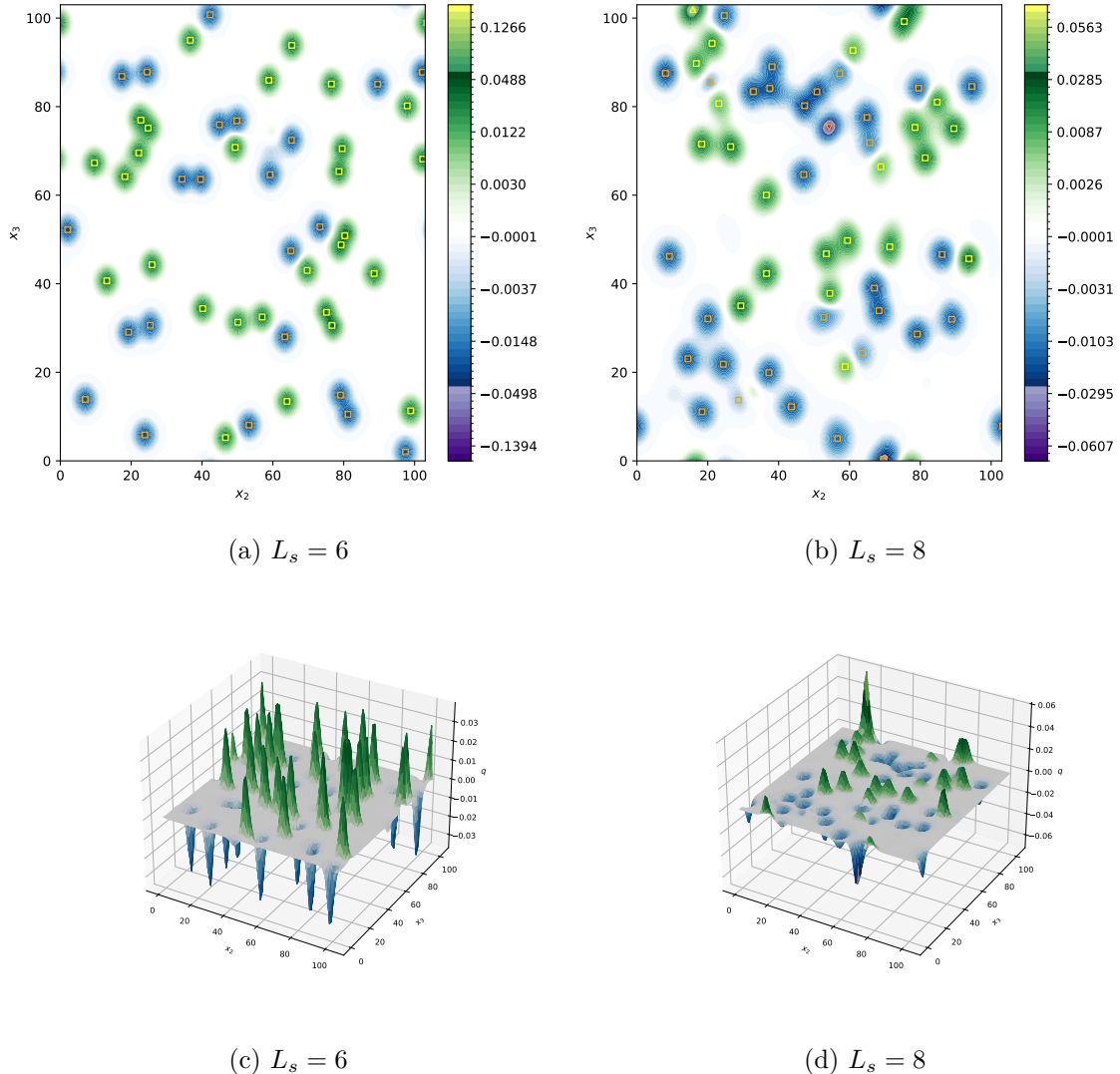


**Figure 4.** Contour plot of topological charge density  $q$  for a single configuration at  $\beta = 2.6$ ,  $t_{gf} = 15$ ,  $L_r = 104$ , and two different  $L_s$ . The result of the identification algorithm is shown in terms of additional markers: boxes indicate fractional instantons (yellow fractional instantons, orange fractional anti-instantons); triangles indicate instantons (yellow instantons, orange anti-instantons).

the moduli coincides with translations, a discrete version of which is also a symmetry on the lattice. This explains their stability under gradient flow.<sup>4</sup>

### 3.3 Fitting topological structures

After a certain number of gradient flow steps, we determine the topological charge density distribution  $q(x)$  on each configuration. In some cases, we also consider the action density.

<sup>4</sup>The stability of such an object is obvious with twist in both,  $T_2$  and  $R^2$ , planes since the topological charge can not decrease below  $Q = 1/N$ , but it also holds in general.

We take either the full four dimensional distribution or sum over both small  $T_2$  directions. Example of the integrated topological charge density for a single configuration is shown in Fig. 4. The distribution clearly shows distinct structures, which should be characterized by relevant parameters and identified with semiclassical objects. As a first step, we identify local maxima in the distribution. These are points, which are larger than all other points in the surrounding area defined by going one lattice spacing in each direction. A more precise location of the maximum can be obtained from a quadratic interpolation. A height distribution can be already obtained from these data, but a more detailed analysis is obtained with fit approach.

Therefore, as a next step, we fit the lattice data around each local maximum. The fit function predicts a maximum (peak) value, its coordinates (not necessarily a lattice point), and a width of the distribution. The expected topological charge profile is known in the case of instantons. Since the sizes of the two planes ( $T_2$  and  $R^2$ ) are very different one might expect anisotropic modifications of the solution. A modified version, which accounts for anisotropies, has been derived in [66],

$$q_4(x) = \tilde{q}_{\max} \left( 1 + \sum_{\mu=1}^4 \left( \frac{x_{\mu} - (x_{\max})_{\mu}}{\rho_{\mu}} \right)^2 \right)^{-4}. \quad (3.1)$$

Integration over the small  $T^2$  directions yields

$$q_2(x) = q_{\max} \left( 1 + \sum_{\mu=2,3} \left( \frac{x_{\mu} - (x_{\max})_{\mu}}{\rho_{\mu}} \right)^2 \right)^{-3}. \quad (3.2)$$

We define

$$Q_I = \frac{\tilde{q}_{\max} \pi^2 \tilde{\rho}^4}{6} = \frac{q_{\max} \pi \rho^2}{2} \quad (3.3)$$

with  $\tilde{\rho}^4 = \prod_{\mu=1}^4 \rho_{\mu}$  and  $\rho^2 = \prod_{\mu=2,3} \rho_{\mu}$ . The BPST (anti-)instanton solution corresponds to  $Q_I = 1$  ( $Q_I = -1$ ) and the same  $\rho = \rho_{\mu}$  in all directions. The deviation from this solution is characterized by the deviation of  $Q_I$  from one and a non-zero excentricity [66], defined as

$$\epsilon = \left[ \sum_{\mu} \left( \frac{\rho_{\mu}}{\rho} - 1 \right)^2 \right]^{\frac{1}{2}}. \quad (3.4)$$

In case of the vortex-like fractional instantons, we lack an analytical expression but can be obtained numerically as explained in Sec. 2.2 and in Ref. [48]. The shape is notably different to the BPST instanton profile. Its integrated shape is more localized than the instanton one, and falls off exponentially at large distances from the center. In any case our fits only affect the behaviour in the vicinity of the center, because they are obtained only from the lattice peak position and its neighbours contained in a local hypercube of side length of two lattice spacings. Thus, using the modified instanton formula we have enough freedom to describe the behaviour of the fractional instanton solution in the neighbourhood of its

center as well which can be seen from Fig. 1. Indeed we have checked that using a Gaussian fitting profile, basically the same results emerge after appropriate rescaling. Thus, for the sake of this paper we have used the modified instanton shape to adjust all the topological structures present in our data.<sup>5</sup> We denote objects with parameters according to (3.3) as instanton-like if  $|Q_I| = 1$ . For vortex-like fractional instantons the fit to this formula has been studied in Section 2. One obtains a value  $|Q_I| \sim 0.6$  close to the value  $1/2$  of its topological charge. In the following we will discuss general properties of the obtained distributions of fit parameters. Some less physical relevant discussions on the gradient flow parameters can be found in Appendix A.

### 3.4 Characterizing the distributions

As a first step, we are now considering the raw distribution of parameters obtained from the fit as shown in Fig. 5 neglecting the excentricity.

BPST instanton contributions are characterized by  $Q_I = \pm 1$ , i. e. the line  $\log(|q_{\max}|) = \log\left(\frac{2}{\pi}\right) - 2\log(\rho)$  in double log representation of the fit results. Similarly one can introduce further lines for contributions similar to topological charge  $Q_I$  using  $\log(|q_{\max}|) = \log\left(\frac{2Q_I}{\pi}\right) - 2\log(\rho)$ . The fractional instantons having  $Q \sim \frac{1}{N}$ , in the dilute situations, extend over the full 2-torus and are therefore expected to be localized at a single point in the diagram as derived in Sec. 2.2. This point is close to the  $Q_I = \frac{1}{N}$  line if the fit is done close to the maximum.

On the lattice, instantons deviate from the continuum BPST solution. At small  $\rho$ , the lattice spacing modifies the profiles and instantons are not resolved below a certain minimal size  $\rho$  in units of the lattice spacing. Large instantons, on the other hand, are affected by finite volume effects in particular related to  $l_s$ . The deviations between the continuum and the lattice versions of semiclassical contributions can be estimated using numerically generated samples of single objects.

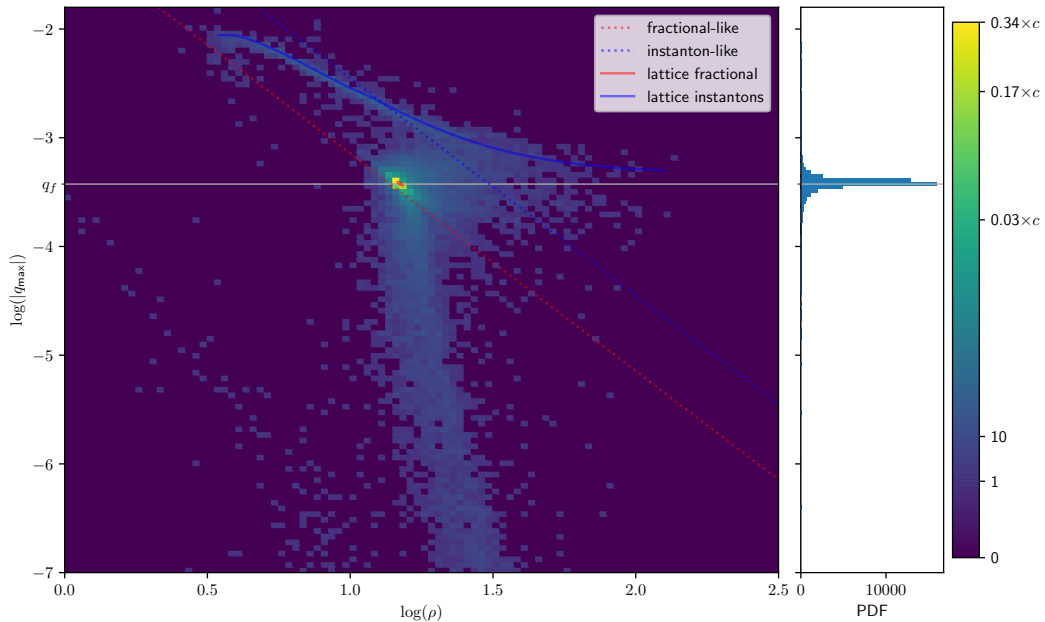
The parameter space of the  $Q_I > \frac{1}{N}$  solutions can be partially explored using the properties of the gradient flow. The Wilson action leads to a decreasing size  $\rho$  and increasing height  $q_{\max}$ , whereas the overimproved flow leads to the opposite effect. Both types of gradient flow move the instanton solution along the line of approximately minimal action, i. e. a lattice counterpart of the continuum BPST line. Increasing the width of the instanton with the overimproved flow, one finally approaches a region where the excentricity starts to increase more rapidly and eventually two peaks of fractional instantons emerge.

At first we discuss the observed distributions of fit parameters in the case of  $L_s = 6$  and  $\beta = 2.6$  before we consider the  $l_s$  dependence. The distributions is shown in Fig. 5. Clearly the majority of the peaks correspond to fractional instantons. A smaller fraction of the distribution can be associated with instantons.

The fractional instanton contributions seems to be extended into two directions: at constant  $|q_{\max}|$  towards larger sizes and at almost constant sizes towards smaller  $|q_{\max}|$ . This can be explained considering neighbouring peaks. If the next neighbour is a fractional

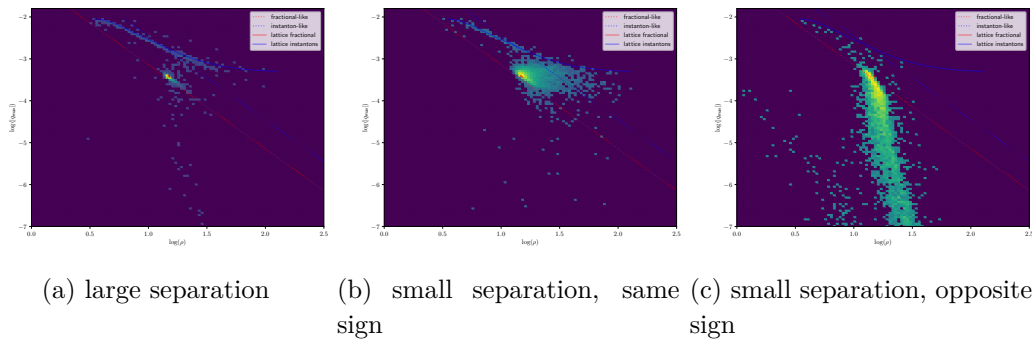
---

<sup>5</sup>We have tested further methods and improvements to account for the different shapes and plan present them in a future publication.

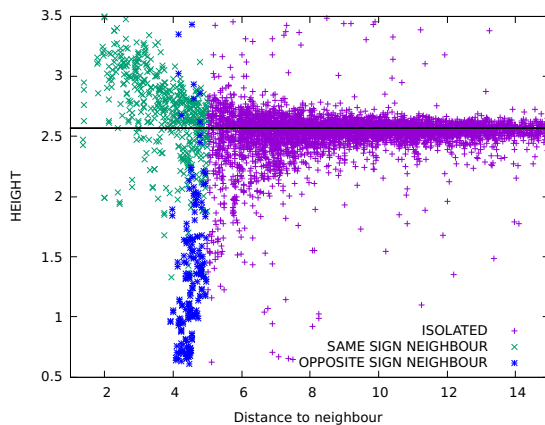


**Figure 5.** Density plot (2D histogram) of the fit parameters obtained from configurations at  $L_s = 6$ ,  $L_r = 104$ ,  $\beta = 2.6$ , and  $t_{gf} = 15$  of Wilson gradient flow. The lattice instanton line is obtained from a single instanton configuration using Wilson and overimproved gradient flow. The upper end of the lattice instanton line corresponds to the point where the instanton dissolves under the Wilson flow and the lower end to the point where the excentricity increases rapidly until two peaks emerge under the overimproved flow. The lattice fractional points result from a fit of a set of configurations with a single fractional instanton generated numerically at  $L_s = 6$  and the vertical line represents the value obtained from (2.12). An exponential map has been applied to the normalization of the 2d histogram as indicated by the colorbar to visualize small densities ( $c$  is the total number of counts). A histogram of the  $q_{\max}$  values is shown on the right.

with the same sign, the width of the peak distribution and the height should increase. On the other hand, if the next peak is of opposite sign, i. e. a fractional anti-fractional pair, the height is expected to decrease. The latter effect is enhanced by the gradient flow, which tends to annihilate pairs of opposite sign. In order to verify this expectation, we separate out the contributions with large distances to the next neighbour (more than one standard deviation larger than the average distance). In addition, we separate contributions with the smallest distances to the next neighbour, which are further separated in the ones with the same sign as the neighbouring peak and the ones with opposite sign of the neighbouring peak. The resulting three distributions of fit parameters are shown in Fig. 6. From these density plots it is clear that well separated peaks follow the expected semiclassical predictions, which are either the BPST instanton line or the fractional instanton profile. If peaks are close to each other there is a significant distortion depending on the relative sign. As expected, the densities at small  $q_{\max}$  can be attributed to pair annihilations. Another illustration of this fact is shown in Fig. 7: at large separations, the distribution is close to



**Figure 6.** Density plot of the fit parameters obtained with same parameters as Fig. 5. This time separated according to the distances and relative sign compared to the next peak. From left to right: peaks with a separation larger than a standard deviation above the average; peaks with more than one standard deviation below the average separation and the same sign; peaks with small separation and opposite sign.

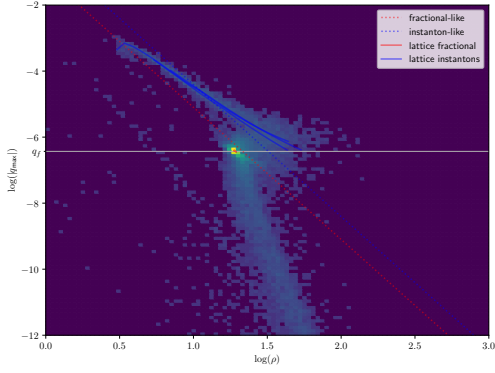
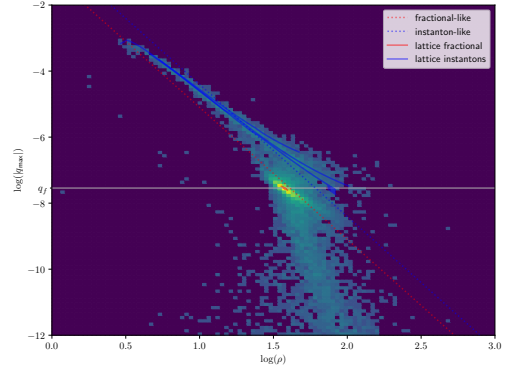
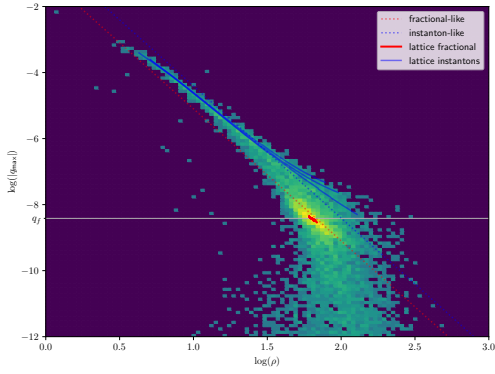
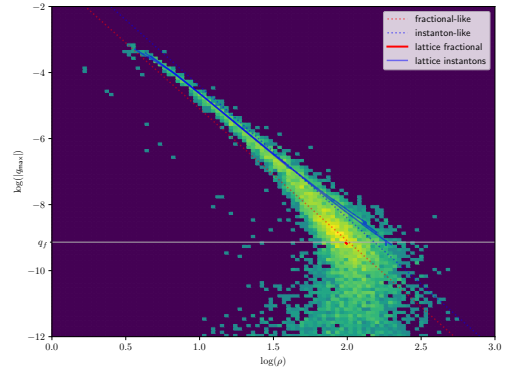
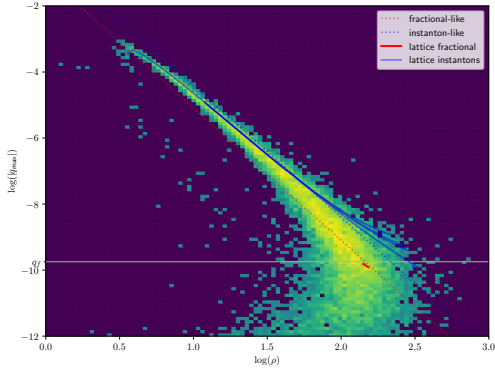
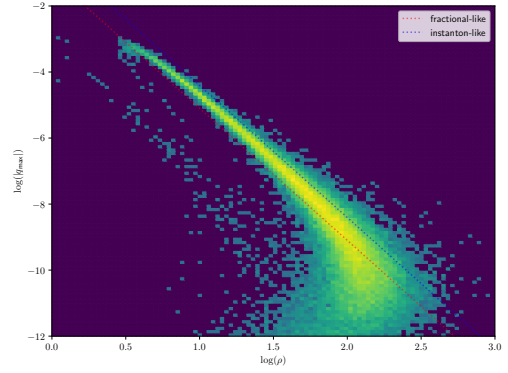


**Figure 7.** Distribution showing the correlation between the height of the peak and distance to a neighbouring peak. Same parameters as Fig. 5, but only for a subset of the configurations. Peaks that are at distance larger than 5 from a neighbour are labelled "ISOLATED". Peaks with nearest neighbours of the topological charge sign (in green) show an increase in height. Those with neighbours of opposite sign (in blue) show a sharp decrease in height.

the expected peak height of a fractional instanton, but there are strong deviations as the separation becomes smaller. The shift in height, positive for equal sign neighbours and negative for opposite sign, is consistent with the effect of overlapping profiles.

The last point in this discussion of the raw fit parameters is a consideration of peak distributions towards the large  $l_s$  limit. This provides only a qualitative picture about the infinite volume limit and more precise quantitative statements are presented in Sec. 4.

At larger  $l_s$ , the integration of the smaller directions in our two-dimensional fit approach (3.2) leads to a distortion and misidentification of densities since there is a non-trivial dependence on  $T_2$ . In order to combine a well-defined large  $l_s$  and small  $l_s$  limit, we apply the following strategy: based on the full four dimensional topological density, we

(a)  $L_s = 6$ (b)  $L_s = 8$ (c)  $L_s = 10$ (d)  $L_s = 12$ (e)  $L_s = 14$ (f)  $L_s = 30$ 

**Figure 8.** Density plot of the four dimensional fit parameters for different  $L_s$  ( $\beta = 2.6, t_{gf} = 15$ ).  $L_r = 104$  for  $L_s < 10$  and  $L_r = 64$  otherwise. The  $q_f$  value corresponds to the prediction of  $Q(0)$  (2.11) in lattice units. In order to estimate the uncertainties of the lattice instanton lines, we have taken three different approximate instanton configurations and deformed them with the overimproved and Wilson flow resulting in three different lines.

perform a four dimensional fit around each peak according to (3.1). At smaller  $l_s$ , this leads to a considerable anisotropy of  $\rho_\mu$  comparing the  $T_2$  and  $R_2$  directions. Therefore, we consider  $\rho$  instead of  $\tilde{\rho}$  which is the geometric mean of only the two  $R^2$  directions.

The density plots for the parameters are shown in Fig. 8. Increasing  $l_s$  the size of the fractional instantons increases. At the same time, the distribution gets broader. Finally, it becomes almost independent of  $l_s$  resembling at  $L_s = 14$  already closely the large volume limit ( $L_s = 30$ ). This is consistent with a picture in which  $\rho$  at small  $l_s$  is determined by the  $T_2$  size, while at large  $l_s$  the distance between the objects determines  $\rho$ .

In Appendix B we add some comments about the distribution for SU(3) and SU(4).

### 3.5 The identification algorithm

Our further discussion of the fractional instanton two-dimensional gas requires an explicit determination of the number of fractional instantons for each configuration. As described in Sec. 3.4, individual peaks can be identified in the distribution of topological charge and characterized by simple fit parameters. There is a natural correspondence between these parameters and semiclassical objects at least for small  $l_s$  and well separated peaks. In this case, fractional instantons can be straightforwardly distinguished from instanton-like contribution and noise, see Fig. 6a. Deformations have to be taken into account due to lattice and finite volume effects. The obvious separation according to (3.3) at the  $|Q_I| = 3/4$  line is hence not a reasonable choice. At smaller distances, the overlap of neighbouring objects introduces additional deformations.

We have tested several different approaches, but the simple separation according to the  $q_{\max}$  already provides a reasonable method to distinguish instantons, fractional instantons, and background noise. In fact, the majority of the instantons have twice the peak height of an isolated fractional instanton and at sufficient gradient flow time, there is also a decent separation from the noise level. It is expected that this simple method is insufficient at larger  $l_s$ . However, the primary focus of the current work is an extensive data scan utilizing straightforward methodology. In a further publication, we plan to consider in more detail improvements at larger  $l_s$ . Note that there is in general a difficulty with large size instantons since, given a limited set of data points, the distribution becomes indistinguishable from a superposition of two fractional instantons.

Hence we apply the following simple algorithm for the identification of fractional instantons: The peaks with a height  $q_{\max}$  larger than two times the expected fractional instanton size are identified as instantons. The expected fractional instanton size ( $q_{\text{frac}}$ ) is determined by a peak in the histogram of  $q_{\max}$ , which is close to the point expected from the considerations of isolated fractionals (2.10). This takes into account possible distortions of the histogram due to the higher density of the objects. We have chosen a sufficient gradient flow time for a decent noise separation. The threshold value  $|q_{\max}| < 20\% q_{\text{frac}}$  determines the neglected remaining background noise peaks.

Errors are estimated by varying upper threshold for the separation between instantons and fractional instantons between  $1.75 q_{\text{frac}}$  and  $2.25 q_{\text{frac}}$  and threshold for the noise level between  $10\% q_{\text{frac}}$  and  $30\% q_{\text{frac}}$ . For illustration, we show the result of the final identification in comparison to the raw topological charge density in Fig. 4. The identification

algorithm is able to distinguish the different contributions and provides a reasonable separation of the objects.

The methods explained in this Section provide the basic input for the discussions of the results presented in the following. Note that in some cases we consider the action density instead of the topological charge density, which due to approximate self-duality, provides a proportional signal. In Sec. 2.4, we discussed the properties of an idealized gas of fractional instantons has been introduced. Most of the calculations were done in the thin abelian vortex approximation (TAVA). This should work quite well in the most dilute situations. In addition now include together with the numbers  $n_+^f$  ( $n_-^f$ ) of fractional (anti-) instantons, also the ones  $n_+^I$  ( $n_-^I$ ) for the ( $Q = 1$  BPST) (anti-)instantons. In some of the observables the  $Q = 1$  instantons can be made equivalent to two fractionals. Hence the correspondence is  $n_+ = n_+^f + 2n_+^I$ ,  $n_- = n_-^f + 2n_-^I$ .

## 4 Analysis of Results

In this Section, we will present our results focusing among the small torus size region. Because of asymptotic freedom, the coupling constant at these scales is small and the simple dilute gas formulas are expected to work better. As the torus size grows, the density of objects also increases until the dilute gas approximation breaks down.

In Section 2 we gave the expected behaviour on the basis of the semiclassical approximation which we are now going to confront with our Monte Carlo results.

### 4.1 Poisson distributed 2D gas of vortex-like fractional instantons

The nature of the 2D gas is particularly neat for the smaller values of  $L_s = 6$  or  $8$  at  $\beta = 2.6$  or higher. We use the  $S_2$  observable which gives the action-density integrated over the directions of the small 2-torus. This gives a distribution of peaks located at different position in the big torus plane. A snapshot of the topological charge distribution of a typical configuration is displayed in Fig. 4. A similar picture is obtained for the action density. Instead of the identification algorithm based on the topological charge, we consider first an investigation using a simple quadratic interpolation of the action density, which can be compared to (2.12).

Analysing a sample of configurations at  $L_s = 6$  and  $\beta = 2.6$  shows a distinctive peak close to the expected location  $H(6) = 2.567 = (100.27 - 283/6^2)/6^2$  according to (2.12)<sup>6</sup>. The histogram of peak heights is shown in Fig. 9 which in the vicinity of the peak is fitted to a Gaussian distribution. The fitted peak position is 2.564(2) and the standard deviation of the Gaussian is 0.088(2). Clearly the distribution is more spread than what the Gaussian predicts, but the precision of the peak location leaves little doubt about the nature of the peak.

The histogram of peak heights has also tails that extend towards higher or lower values. It is important to understand the origin of these deviations in this simple situation since it can help to extend this interpretation to situations occurring at much higher densities.

---

<sup>6</sup>Notice that on the lattice one measures the value of the  $S_2$  integrated over a plaquette which is  $S_2/L_s^2$ .

Indeed, this was already discussed in the previous section and illustrated in Fig. 7. There we see that peaks at a distance larger than 5 lattice spacing from a neighbour (in purple) are giving the narrow Gaussian distribution around the expected value. Those closer to a neighbour are split into two sets: if the neighbour has the same topological charge sign (in green) the height tends to higher values. This is easily explained by the overlap of the contributions. The remaining set corresponds to peaks having a closest neighbour of opposite sign (in blue). In this case we observe that as the distance becomes smaller there is a strong neutralization of the signal leading to a much smaller peak height. We think that this explains very neatly the origin of the extended tails in Fig. 9.

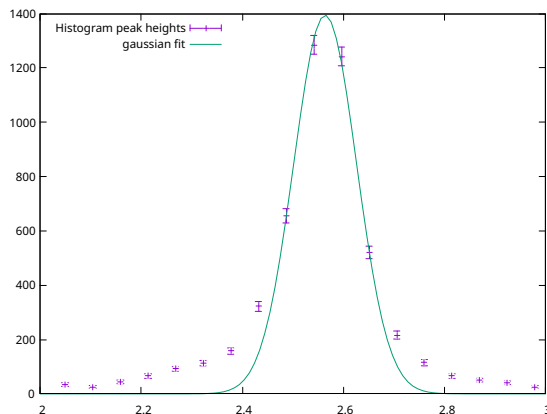


**Figure 9.** Histogram of the action density peak heights  $H_0$  at  $L_s = 6$ ,  $\beta = 2.6$ ,  $6^2 \times 10^4$  lattice. This corresponds to wider range histogram of the topological charge density (log scale) shown in Fig. 5.

Now we proceed to test the remaining aspects of the distribution itself: its Poisson nature and the 2D spatial distribution. The latter is crucial to show that the FI are indeed independent and do not cluster into molecules which, as mentioned earlier, would kill its effect on the string tension.

The characteristics of the trinomial/Poisson distribution was described in Sec. 2. Although we gave analytic formulas for most distributions we have also used a numerical method to determine the predictions of a 2D gas of fractional instantons. Giving as input only the density one can generate hundreds of thousands of configurations in very short times following the probability distribution explained in Sec. 2 and setting the minimum area  $A_0$  to a plaquette and the total area to the corresponding one in the lattice simulation. Once a FI or AFI is created in a given plaquette, its location is generated uniformly with this plaquette. One can easily add the constraint of having only an even total number of objects (integer  $Q$ ). In this way all distributions can be determined in terms of a single parameter, the mean number of objects, which can be adjusted to match the set of configurations one is trying to compare with.

Let us now proceed to compare the distributions obtained by analysing the Monte Carlo generated configurations with the analytic and numerical ones of a free 2D gas. We take as an example the case of  $L_s = 6$  and  $\beta = 2.6$  for which the density is relatively small.

Let us first study the histogram that gives the distribution of the number of objects (FI and AFI). Since the lattice configurations have been obtained with no twist in the big plane we expect only an even number of objects (FI+AFI) per configuration. Unfortunately our peak-identification method has an uncertainty and odd numbers are also found, although in a smaller proportion. Nonetheless, this uncertainty in the number of peaks is much smaller than the dispersion of the distribution. This can be seen in Fig. 10 where we take a bin size of 2 which adds up the even and odd values.

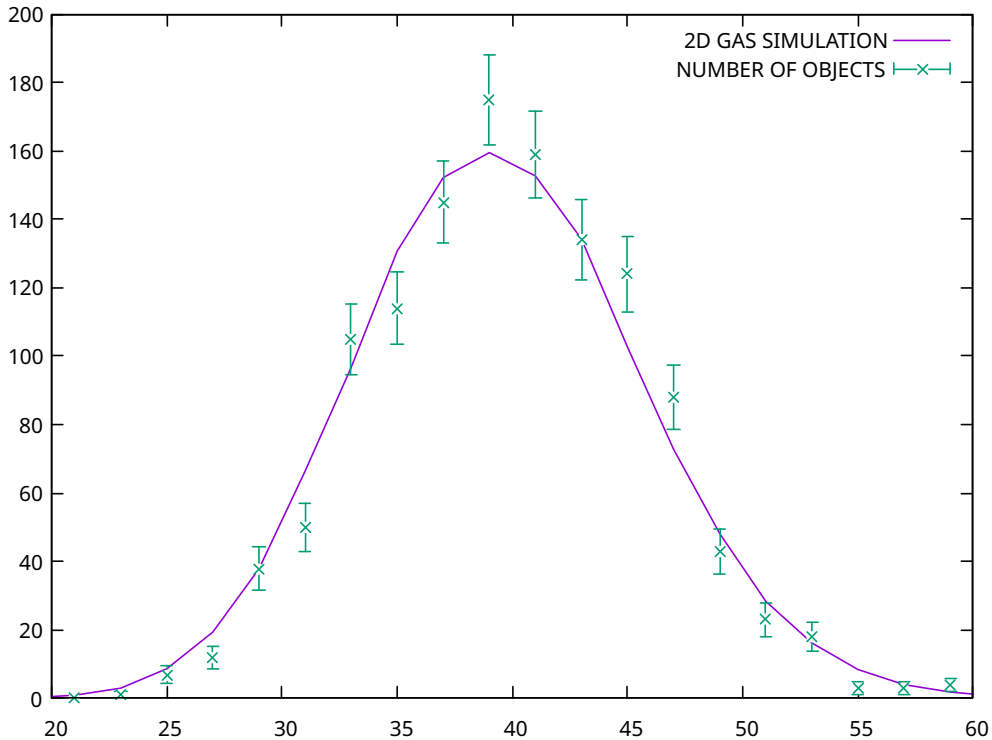


**Figure 10.** The plot compares the histogram of the number of objects with the prediction of the 2D Poisson gas (see text) for  $L_s = 6$ ,  $\beta = 2.6$ .

The actual data points are compared with the results of the 2D gas, drawn as a continuum line. Since by construction, the 2D gas result has no odd number of objects, we use also the same bin size of 2 for this case. The matching is very good and the only input for the 2D gas is that the mean number of objects matches the Monte Carlo configurations.

Another interesting piece of information is the distribution of minimum distance to a neighbouring peak. As will be argued later this distribution can be used to measure the effect of the flow as well as the possible interactions (attractive or repulsive) among the objects. For that purpose it is interesting to distinguish the cases in which the closest neighbour has the same or opposite sign of the topological charge. For the Poisson gas the two distributions are essentially equal.

As an example we consider again the case for  $L_s = 6$ ,  $L_t = 104$  and  $\beta = 2.6$ . The histogram of distances is shown in Fig. 11. The actual data are split into distance to an

object of equal sign (left plot) and to opposite sign (right plot). The results are compared to our analytic formula for a 2D Poissonian gas distribution

$$2Ax e^{-Bx^2} \quad (4.1)$$

The value of  $A$  and  $B$  are extracted from a fit for distances  $30 > x > 15$ . The results are quite informative. For the equal sign case, the value of  $B$  corresponds to a density of  $\rho_{2D} = 0.00359(4)$ , while the actual measured density is  $\rho_{2D} = 0.00362(3)$ . The total normalization is also consistent within errors. The curve matches very well with the data at large distances. For  $d < 15$  there seems to be a small depletion at short distances compensated by a small enhancement at intermediate distances. It is hard to know if that is the result of the overlapping of profiles, a consequence of the peak selection or a genuine hard-core repulsion among structures. Notice that the prediction is based on the thin vortex approximation, while our objects have a size.

The opposite sign distance distribution is very different. The fit is also good at large distances but the extracted value of  $B$  corresponds to a density of  $\rho_{2D} = 0.00328(6)$  which is somewhat smaller than the measured one. Furthermore, the overall integral of the curve is 17% higher than the actual number of pairs. This can be seen as a decrease of the expected neighbouring opposite sign pairs at short distances. There are two related effects that can contribute to this phenomenon. On one side, there might be a reduction of pairs due to FI-AFI annihilation, a phenomenon to be expected as a result of the flow. Another possible effect is the strong decrease in peak height observed for close opposite-sign pairs, as shown in Fig. 7, making it harder to distinguish from low amplitude noise.

Notice that even in this rather dilute case the peak of the distance distribution is at 10 in lattice units which is less than twice the size of the small torus (The prediction of our formulas is  $1/\sqrt{\pi\rho_{2D}} = 9.38$ ). Furthermore, in  $\sim 18\%$  of all cases the distance is equal or smaller than 6, which would certainly alter the 2D shape of the object.

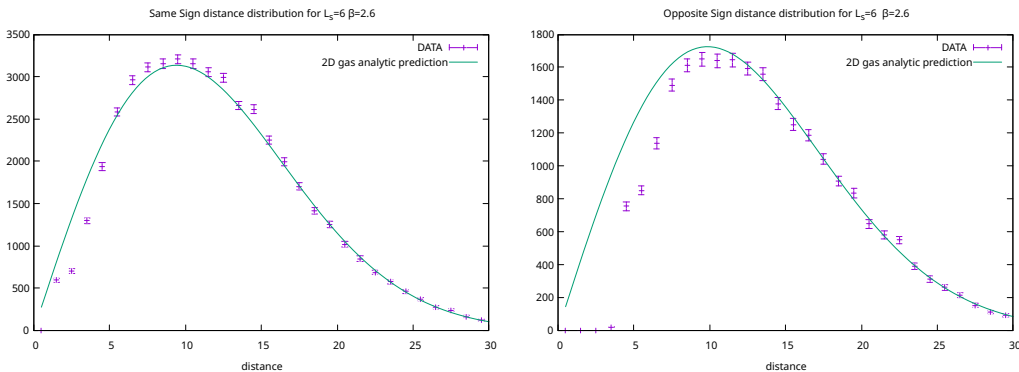


**Figure 11.** Distribution of minimum distances from one object to the closest one depending on whether the closest neighbour has the same or opposite sign of topological charge (for  $L_s = 6$ ,  $\beta = 2.6$ ). This is compared with the predictions of the Poissonian 2D gas (see text).

The situation gets worse as the density increases. For example for  $L_s = 10$ ,  $L_t = 64$  and  $\beta = 2.6$ , our formulas give a peak of the minimum distance distribution at 7.39, which

is less than the actual torus size of 10. It is clear that we expect a large number of cases with modified shapes due to the distortion induced by the neighbours. As we saw before, this would contribute to the spreading of the height distribution.

Another interesting distribution is that of the topological charge. The predictions of the 2D free gas of fractional instantons were given in Sec. 2. This quantity can be measured directly as the integral over the topological charge density and compared, configuration by configuration, with the result of adding the integer or half integer charges of both instantons and fractional instantons that result from our identification. This provides a test that the identification is correct. For our standard  $L_s = 6$   $\beta = 2.6$  we display in Fig. 12 the observed distribution using both methods compared with the distribution generated by our 2D gas simulation.

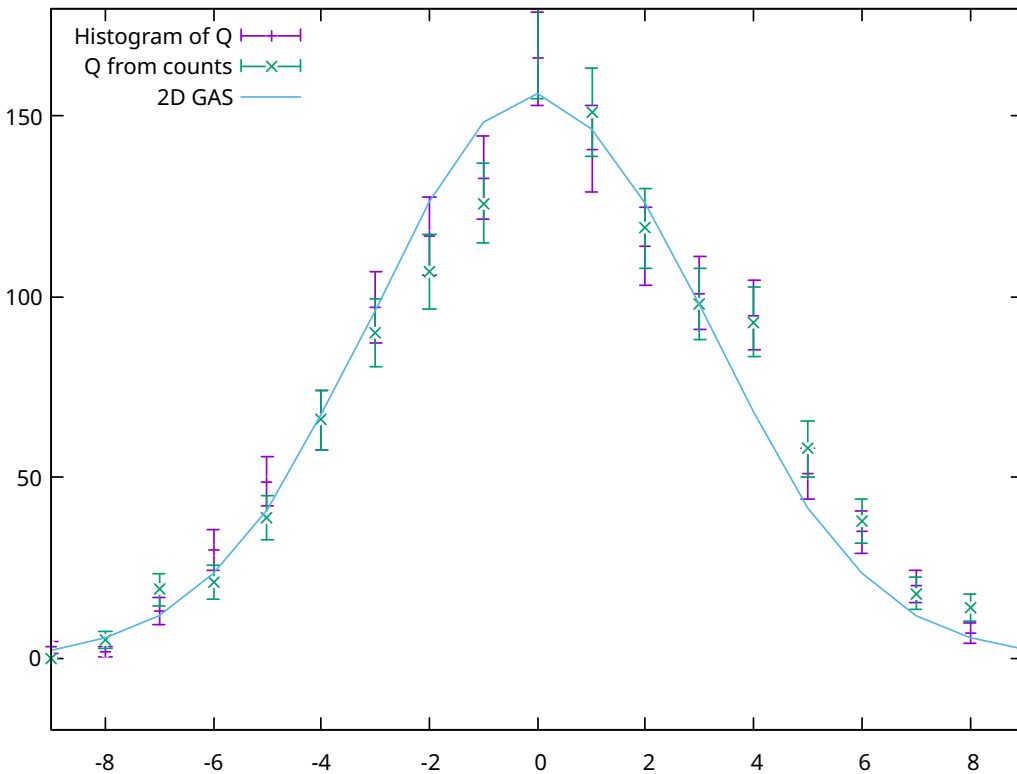


**Figure 12.** Histogram of topological charges measured in our configurations at  $L_s = 6$   $\beta = 2.6$ . The two sets of data points come from a direct measurement of the topological charge or by summing up the charges of the objects identified by our methods. The continuous line is the result of our 2D gas simulation.

#### 4.2 Density evolution as a function of $\beta$

We will now confront our results concerning the evolution of the density of FI and AFI as a function of the lattice coupling at fixed value of the small torus lattice size. The semi-classical prediction on the lattice implies that the density is proportional to the probability

of creating a fractional instanton, which is proportional to the Boltzmann weight times a prefactor related to the number of zero-modes of the adjoint Dirac operator (4 in our case), as follows

$$A(L_s) \beta^2 \exp\{-\beta S_L(L_s)/4\}, \quad (4.2)$$

where the FI lattice action  $S_L(L_s)$  approximates the continuum result of  $4\pi^2$  and its value can be obtained from the studies of a single FI given in Section 2. Notice that Eq. 4.2 is the same one that was used long time ago to analyse the density of kink-like fractional instantons that appear in a  $T_3 \times R$  study [67]. Instead of comparing the density itself we will plot the 2D diluteness observable  $D(L_s, \beta)$  (defined in Eq. (2.28)) which is dimensionless but obviously has the same  $\beta$  dependence up to a change in the numerical prefactor  $A(L_s)$ . We will focus on the region of diluteness less than 1, where one expects the semiclassical approximation to work better. Our results are given in Fig. 13 and cover a large range of values of the diluteness and of  $\beta$  and  $L_s$  values. For the calculation  $Q = 1$  instantons are counted as 2 fractional instantons.

The lines are the results of a one parameter fit to Eq. (4.2). Only the values of  $\beta > 2.5$  have been fitted and the resulting  $\chi^2$  values are of order 1. For smaller  $\beta$  there is a small excess. Notice that the data points follow very closely the fit lines which look like parallel straight lines, because they are dominated by the exponential dependence. The agreement is very remarkable and extends also up to rather large values of  $L_s$ .

The values of  $A(L_s)$  resulting from the fit should approach the predictions of the leading order renormalization group as explained in the theoretical discussions of Sec. 2.6. In the left part of Fig. 13 we plot the resulting values in a log-log plot. We fit the values of  $A(L_s)$  to a power of  $L_s$  which shows as straight lines in this plot:

$$A(L_s) = A L_s^\alpha \quad (4.3)$$

The fit is very good having  $\sqrt{\chi^2} = 0.9$  and giving an exponent  $\alpha = 3.45(2)$  which is remarkably close to the prediction of leading order renormalization group  $11/3 = 3.67$ . The fit gives the value of the coefficient  $A = 3.91(10) 10^6$ .

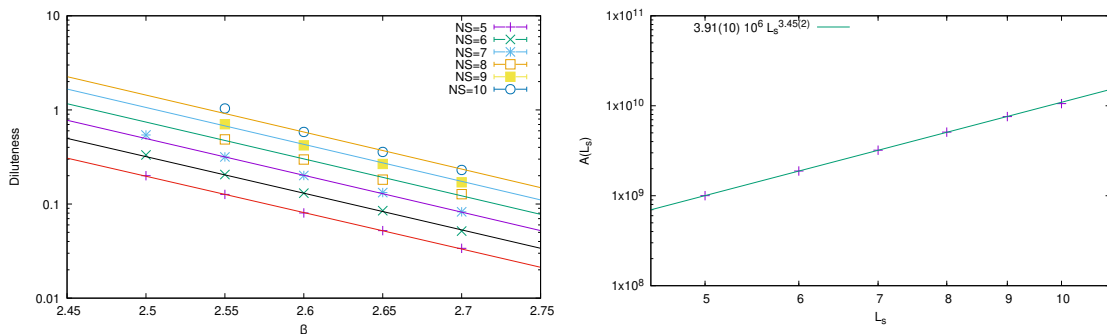


**Figure 13.** Comparison of the measured value of the diluteness  $D(L_s, \beta)$  with the semiclassical predictions. LEFT: Comparison of the data with the beta dependence in Eq.(4.2). RIGHT: Dependence of the prefactor with  $L_s$  and fit to Eq. (4.3).

In summary, our data of low diluteness and high  $\beta$  values follows the semiclassical predictions on the lattice and in the continuum.

Another way to show that our results are actually continuum results is to express the density  $\rho_{2D}(l_s)$  as a function of the torus size  $l_s$ , both expressed in physical units. This is displayed in Fig 14. Notice that the results scale very well at low values of the density and for  $\beta > 2.5$ . Deviations appear at larger values while deviations at small  $l_s$  are due to lattice artifacts introduced once the small size of the  $T_2$  box gets closer to the scale of the lattice spacing.

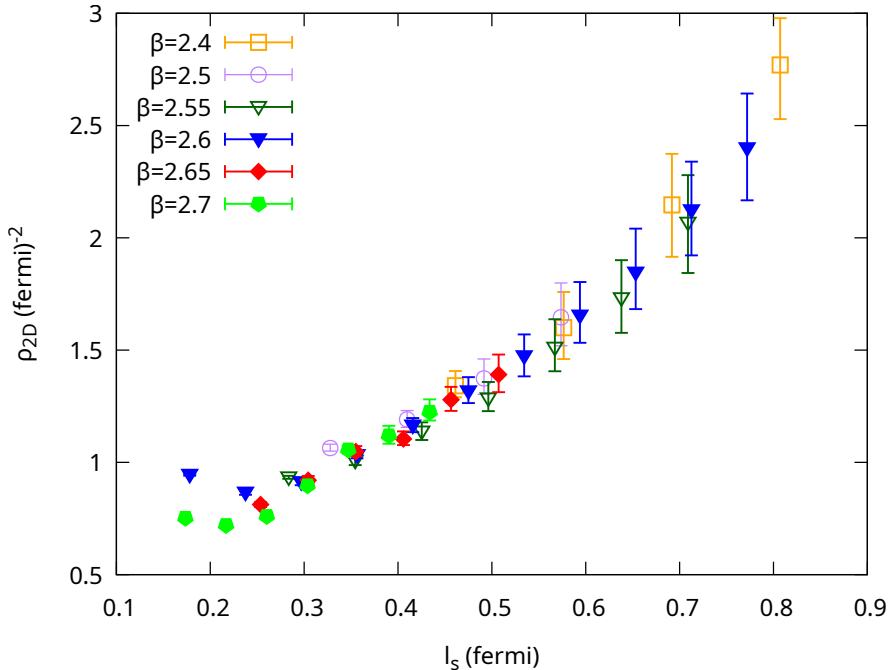


**Figure 14.** Evolution of the density of objects  $\rho_{2D}$  with the physical torus size  $l_s$ . Instantons are counted as two fractional instantons. The error bars contain the systematic part coming from the identification algorithm as explained at the end of Sec. 3.5

### 4.3 Relation with the string tension

In this subsection we show our results concerning Creutz ratios and string tension. Our goal is to verify the predictions of the semiclassical formulas which establish a relation between the two-dimensional density of fractional instantons and the string tension. The string tension in lattice units is given by the infinite size limit of square Creutz ratios. It is clear that this limit cannot be attained at finite volume. There are indeed distortions to the area law when the size of the loop approaches the size of our large torus. Thus we are limited to analysing square Creutz ratios  $\chi(R)$  up to sizes at most one fourth or one fifth of the size of the large torus. On the opposite hand, the value of  $R$  should not be smaller than  $L_s$  since that is the size of the fractional instanton at low densities. In Fig. 15 we

display the effective string tension in physical units, defined as the average of Creutz ratios in the interval  $R \in [1.1l_s, 2.0l_s]$ , as a function of  $l_s$  in fermi. Although the results show a certain degree of dispersion the growth with  $l_s$  is obvious. For comparison we include a horizontal line which marks the value of 5 fermi<sup>-2</sup> corresponding to the infinite volume string tension used as a unit for the lattice spacing.

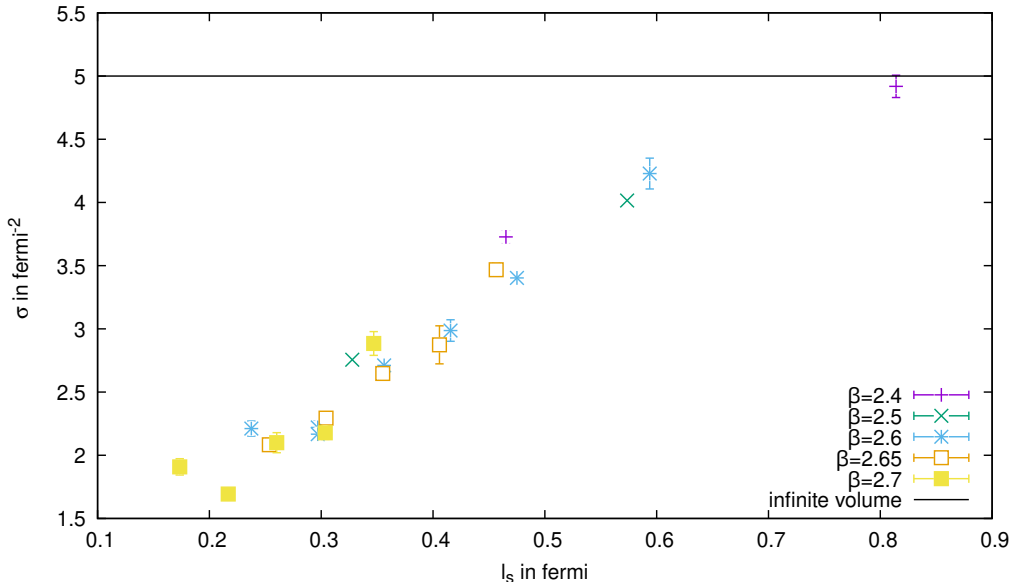


**Figure 15.** Effective string tension defined through Creutz ratios (see text) as a function of the 2-torus size  $l_s$ . This has been obtained at the flow times of Tab. 1.

The simple Thin Abelian Vortex Approximation (TAVA) predicts that the string tension is given by two times the density of fractional instantons. To test this, we compare the effective string tension measured from Creutz ratios as explained above with the density of fractional instantons and anti-instantons. A nicer plot is obtained if we multiply both the density and the string tension by  $l_s^2$ . Our results are plotted in Fig. 16. The horizontal axis, labelled fractional diluteness, is given by the 2D density times  $l_s^2$ . We emphasize that  $Q = 1$  instantons are not included in the count. The linear correlation of the two quantities is obvious from the figure. However, the best fit to the proportionality constant is 2.89 rather than 2. This can be due in part to the fact that the range of Creutz ratios is rather small and the effect of the finite size of the fractional instantons shifts these to a value between 2 and 2.4, as verified in our measurements on smooth configurations. The higher value might indicate that the density has been reduced due to annihilation of pairs during the flow (we will see the effects on the flow in the following section).

The results that we have presented show two remarkable facts. First of all, the fact that the effective string tension appearing in Fig. 15 at  $l_s \sim 0.8$  fermi is indeed very close to the value of the string tension at infinite volume. On the other hand we have clearly shown that the very same effective string tension is proportional to the density of fractional instantons. It is the combination of these two facts that was taken as an indication that the

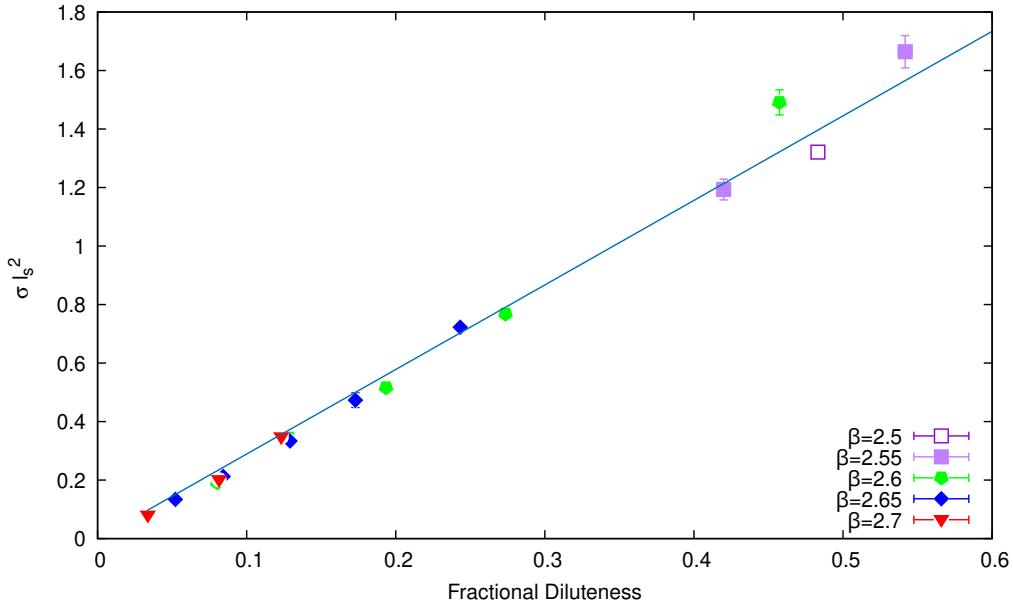


**Figure 16.** Plot of the effective string tension versus the 2D density of fractional instantons. Both quantities are multiplied by  $l_s^2$ . The continuous line is  $2.89 x$ . (Results at flow times of Tab. 1)

Confinement property of the infinite volume theory has its origin in fractional instantons.

Nonetheless, we realize that our estimates of both the string tension and densities are subject to corrections of different nature which should be clarified. We already emphasized that our estimate of the string tension is based on Creutz ratios which are not asymptotically large. This is expected to give estimates that are larger by 10 to 20 % (as we learned from the smooth configuration Fig. 2). A much more important issue is the effect of the flow. This is expected to reduce the number of objects altering the densities. For the overimproved flow the reduction comes mainly from annihilation of nearby fractional instanton-antiinstanton pairs. For Wilson flow one also expects the evaporation of small instantons, although this is not expected to affect the string tension. In the next subsection we will analyse these effects.

#### 4.4 Flow dependence of the results

Indeed, it is possible to compute the string tension for the configurations directly without the flow. There are various ways in which this can be done. A rather standard way led to the results presented before in Fig. 3. From this Figure it is clear that the string tension grows for small torus sizes and seems to stabilize to its infinite volume value at  $l_s \sim 0.8$  fermi, in agreement with our measurements done on the flowed configurations. One can also compute the string tension from square Creutz ratios  $\chi(R)$ . The procedure is to extrapolate the results to infinite size. In the standard infinite volume case the Creutz ratios show a linear dependence in  $1/R^2$  for large enough sizes with a coefficient which is not far from  $\pi/6$ , which is the expected Lüscher term [68] arising universally from the transverse fluctuations of a string with contour on the Wilson loop. One expects the behaviour to be

modified in our setting for large values of  $R$  and small torus sizes  $l_s$ , since the fluctuations are bounded. In the absence of a more precise formula, we have simply performed a linear and a quadratic fit to the square Creutz ratios  $\chi(R)$  as a function of  $1/R^2$ . The results are collected in Fig. 17. Errors are big because large Creutz ratios are very noisy quantities,

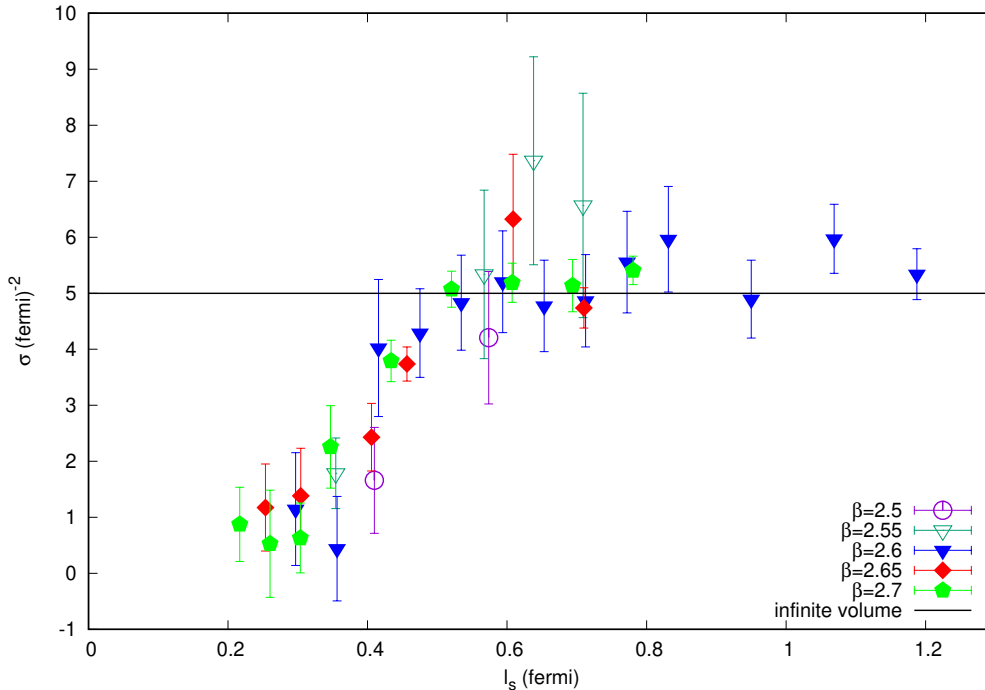


**Figure 17.** Evolution of the string tension with  $l_s$  as obtained at zero flow time from Wilson loops and Creutz ratios APE-smearred over the directions transverse to the plane of the loop ( $t_{gf} = 0$ ).

but it is clear that the results are consistent with the previous estimates. Using alternative methods, which assume a certain form of the static quark anti-quark potential, one obtains similar results presented in Fig. 3. Once more at around  $l_s \sim 0.7$  fermi the string tension reaches a value which is very close to the asymptotic one.

Another alternative calculation makes use of the technique employed in Ref. [69] which gave very good results. The idea is based on the fact that Creutz ratios are lattice approximations to the double derivative of the logarithm of the Wilson loop. These are ultraviolet finite observables. Hence, one expects that if one applies gradient flow for very small times  $\tau$ , it is possible to extrapolate back to zero flow time without the occurrence of singularities. Furthermore, even at very small flow times the fluctuations of the Creutz ratios are strongly suppressed. The question then is what is the correct functional dependence to be used for the extrapolation. In the continuum within perturbation theory the flow time  $\tau$  introduces a damping of momenta in propagators of the form  $\exp\{-\tau p^2/2\}$ . Creutz ratios are indeed computable in perturbation theory and one can use the flowed perturbative formulas to predict the  $\tau$  dependence of the ratios. The resulting formula has the form

$$\chi(R, \tau) = \chi(R, 0)(1 - e^{-b/\tau}) \quad (4.4)$$

This shows a plateau and then a decrease. We fit our ratios to this formula within a region in which the ratios have only decreased by a few percent. Typically this occurs when the smearing radius  $\sqrt{8\tau}$  is  $0.1-0.5R$ . Still, the decrease in statistical errors is dramatic. The resulting  $\chi(R, 0)$  values are treated in the same way as the ones obtained directly. Unfortunately the method requires storing the evolution of all Creutz ratios and configurations for the corresponding interval of flow times. Thus, we used the method only as a test for a reduced sample of configurations and parameters. The results are given in Fig. 18. The displayed errors include both statistical and systematic added in quadrature. The latter are estimated by the spread of the results as applied to both smeared and smeared Wilson loops. The values seem to be slightly higher than the ones obtained previously with other methods, but the pattern is the same: there is a rise of the string tension with  $l_s$  ending at around 0.7 fermi. The values then flatten and seem to tend smoothly to infinite volume. Notice that we have added the result obtained at  $L_s = 30$  corresponding to  $l_s \sim 1.8$ . The value there is slightly higher than the nominal value of  $5 \text{ fermi}^{-2}$ , but this value is taken by results of other authors which have errors of similar size.

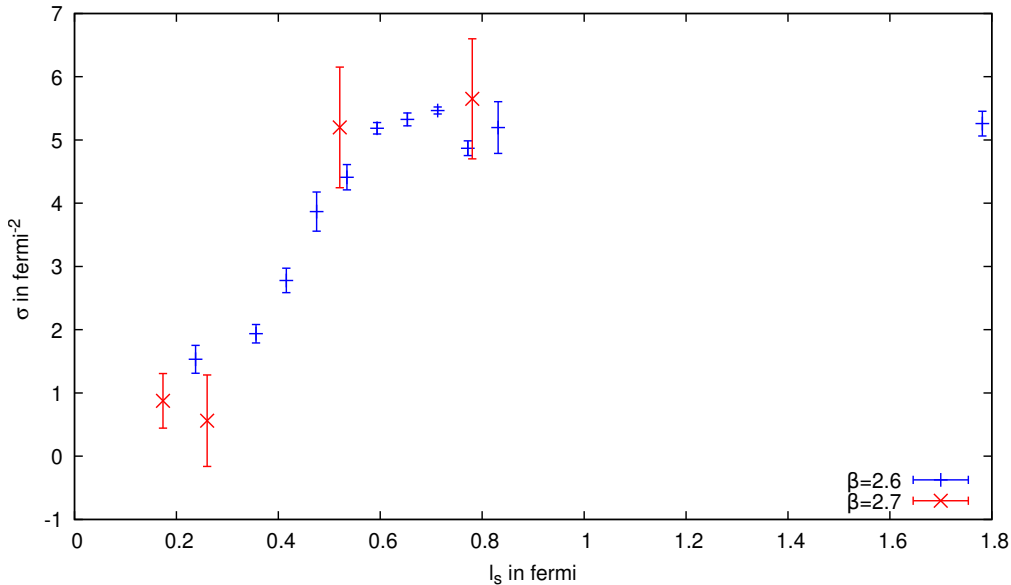


**Figure 18.** String tension as a function of  $l_s$  as obtained by extrapolation of the flowed Creutz ratios to zero flow time.

As we have seen, within the errors of our estimates, the flow has a rather small effect on the string tension shape and values. A much more delicate point is how does the flow affect the density of fractional instantons. It is certainly expected that the density decreases with the flow time. This follows from the mechanisms described earlier in subsection 3.2: Pair annihilation and fusion and evaporation of  $Q = 1$  instantons. The latter aspect does not affect the density of fractional instantons, but fusion does. For Wilson flow one expects that nearby pairs of equal sign fractional instantons fuse to produce a single  $Q = 1$  which does not contribute to the density.

It is impossible to perform a measurement of the density at zero flow time, since the signal is completely covered by the low frequency noise. However, what we can do is to monitor how the density depends on the flow time to pin down its effect on the correlation between this density and the measured string tension. For this purpose, we made a detailed study on the gradient flow dependence for a particular set of ensembles. The results are collected in Fig 19. As expected, the fractional instanton density decreases monotonically with the flow time  $t_{gf}$ . At small flow times, the errors are quite large, and tend to give much higher values because the configurations are polluted by noise which is misidentified as fractional instantons. For large flow time, the noise has decreased enough such that the identification algorithm performs well. The mild dependence left at large flow time is due to the effects mentioned above. From Fig. 19 we can see that our choice of  $t_{gf} = 15$  for  $\beta = 2.6$  in Tab. 1 is such that we end in the region where the  $t_{gf}$  dependence is mild even for still quite large torus size  $l_s \sim 0.6$ .

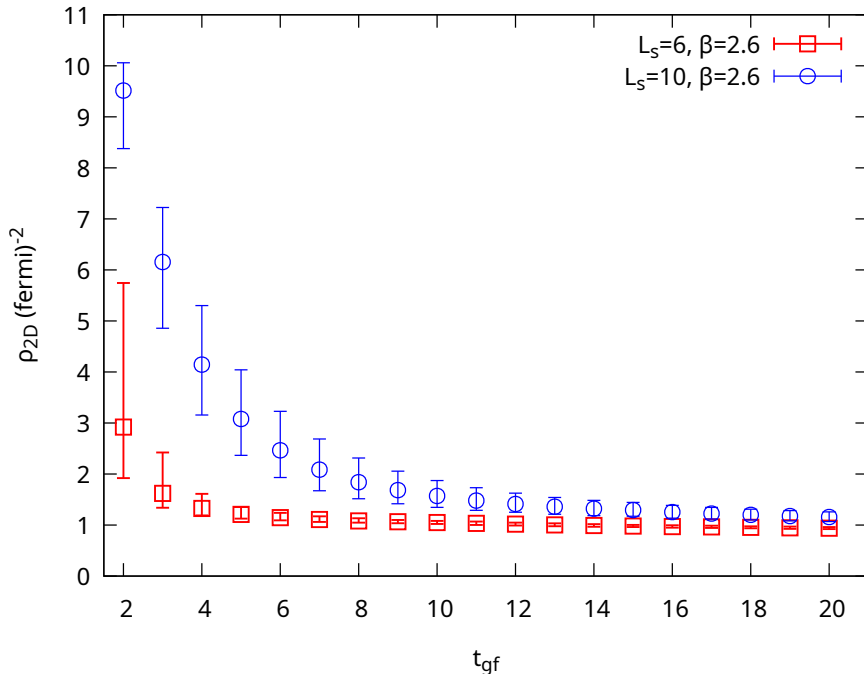


**Figure 19.** Dependence of the fractional instanton density  $\rho_{2D}$  on the flow time  $t_{gf}$  for two different ensembles at  $l_s = 0.24$  for the small lattice and  $l_s = 0.59$  for the large one.

For these ensembles we have also measured the string tension by means of the average of Creutz ratios of size  $R \in [1.1, 2]l_s$  for various values of the flow time. The ratio of this result with the density is depicted in Fig. 20 for one of the ensembles at the larger value of  $l_s$ . Despite the big change in density, the ratio shows a rather mild growth. Indeed, this growth is consistent with the interpretation given earlier to the rather large slope obtained in Fig. 16 at  $t_{gf} = 15$ . The ratio at smaller flow times comes closer to the expected value slightly above 2.

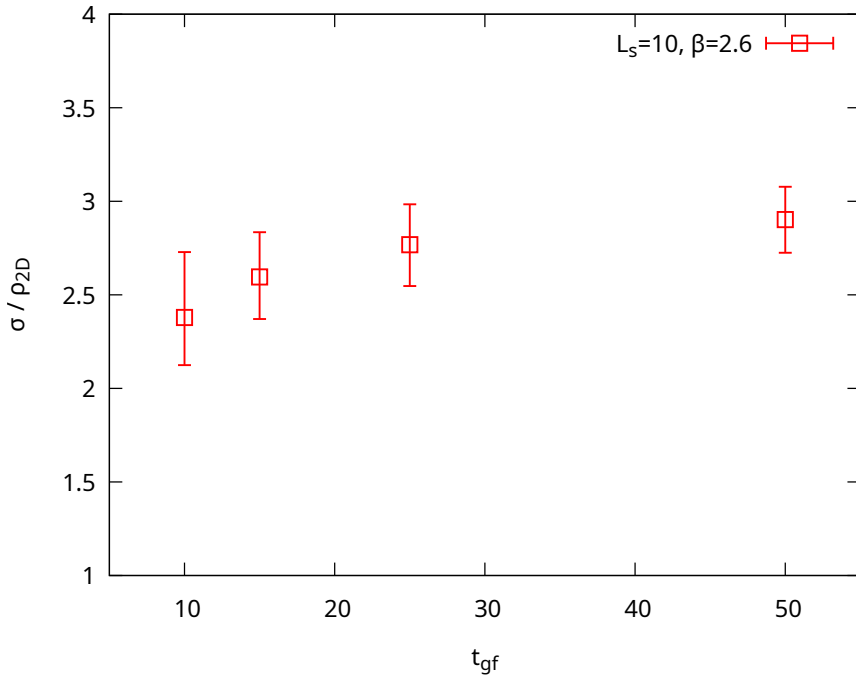


**Figure 20.** Flow time dependence of  $\sigma/\rho_{2D}$ , the ratio between the effective string tension and the fractional instanton density. The plot shows that the ratio grows rather mildly during the flow, thus exhibiting a strong correlation between the two quantities.

## 5 Going to larger torus sizes

In the previous sections we have studied the evolution of the Yang-Mills system in  $T_2 \times R^2$  as a function of the size of the torus. Our results have concentrated upon the low density regime where one expects the semiclassical predictions to hold. We have verified that this is indeed the case by checking the various distributions and observables. As the size grows, the density increases and our results predict when the gas ceases to be dilute. This occurs as the size becomes roughly larger than the 0.6 fermi. This matches with the estimate made many years ago [22, 24] when studying the evolution within a  $T_3 \times R$  geometry. Extending the study of the system beyond that point is very important in order to relate the understanding developed in the semiclassical analysis with the behaviour of the system at infinite volume. In particular, our previous study has traced the origin of a non-zero string tension to the presence of fractional instantons that behave as center vortices and induce Confinement. Interestingly enough at the edge of the semiclassical region the value of the string tension is not far from the value measured at infinite volume by other research groups. It is this similarity and the subsequent mild evolution of the string tension towards its infinite volume value that led one of the present authors and his students to propose a possible explanation [24] that can be referred to as Fractional Instanton Liquid Model (FILM). It is important to review the main elements of the proposal to determine what specific predictions arise from this scenario in studying the evolution at larger torus sizes.

The quantum fluctuations imply that larger fractional instantons are more probable than small ones. This is not surprising since the same happens for instantons, as established by 't Hooft in his famous semiclassical analysis [44]. However, the maximum size is limited by the torus. Thus, within the semiclassical regime the fractional instanton fill the torus completely and they simply become more dense as a 2D gas. However, as the gas ceases to be dilute the distance among objects becomes competitive with the torus size and the anisotropy of the distribution starts to disappear. It is to be expected that eventually the distance among objects is a physical scale determined in terms of the characteristic scales of the theory, like the Lambda parameter, and decoupled from the physical size of the geometrical container. It is in this way that one can understand that the result tends to a limit at infinite volume and isotropy is recovered. It makes a lot of sense that this occurs rather quickly once the gas ceases to be dilute.

Notice that fractional instanton do not exist isolated (i.e. surrounded by the classical vacuum) so that their size is directly connected to the distance to its neighbours. In the dilute setting the neighbours are the replicas induced by the torus geometry, but in the non-dilute case the closest neighbours might come from all directions. The picture that emerges as the size becomes larger is that of a 4D liquid.

In the present work we have monitored both the size and the distance between the fractional instantons as a function of the torus size in physical units. Our results are collected in Fig. 21. On the left plot we can see how at the edge of the semiclassical regime  $l_s \sim 0.7$  fermi, the size of the fractional instantons departs from the naive linear dependence  $\rho \sim l_s$ . In fact, it seems that this size  $\rho$  couples to the mean distance between topological objects, displayed in the right plot. Furthermore, this distance seems to scale and flatten out in physical units in agreement with the expectations of the model.

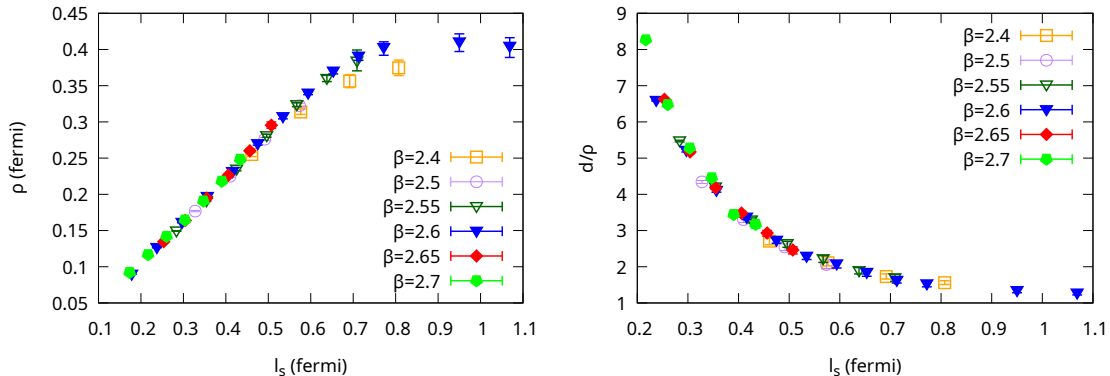


**Figure 21.** LEFT: Evolution of the size of the fractional instantons  $\rho$  as a function of the size of the  $T_2$  box  $l_s$ . In this case we discarded completely the contribution coming from the instantons as they have a different parameter space. RIGHT: Evolution of the mean distance between fractional instantons and their size. The data hints that at large  $l_s$  the size of the fractional is given by their mean distance  $\rho \sim d$ .

Unfortunately, our methods of identification of fractional instantons rely heavily on the

height distribution of the 2D integrated profile  $S_2$ . This is highly inadequate to study the 4D liquid distribution expected to hold at larger torus sizes. Four-dimensional topological charge/action density heights, sizes and distance to neighbours have to be used for a proper identification in this new context.

There is an additional difficulty because at high densities the proportion of ordinary  $Q = 1$  instantons grows. However, one can still think of these instantons as overlapping pairs of fractional instantons. Instantons of much smaller size can still appear, but they are suppressed by having a smaller quantum weight. In any case distinguishing  $|Q|=1$  instantons from fractional instantons remains a challenge. One might still use the ratio of action per peak as an indicator of the percentage of fractional instantons versus instantons as was done in the  $T_3 \times R$  case [25].

Another technical complication which becomes very relevant at high densities is the method used to suppress high frequency quantum fluctuations. We have commented about the effects of Wilson flow and using alternatives is particularly relevant for the high density case.

Concerning the main observables there are also important changes. It is clear that the density of fractionals have to be computed in 4D  $\rho_{4D}$  instead of 2D. Thus, at fixed lattice spacing and large torus size, the number of fractionals should grow like  $L_s^2$ . One has also to revisit the expected relation between the density of fractional instantons and the value of the string tension. Given a large Wilson loop one can fix the minimal 2D surface having the loop as boundary, having area  $A$ . It is really the number of fractional instantons cut by this surface what really matters for the calculation of the expectation value and assuming a fixed fractional instanton size  $l_I$ , this number should be proportional to  $l_I^2 \times \rho_{4D} \times A$ . Still the surface will sometimes cut the fractional instantons at the center and sometimes at the edge. It is also much more doubtful that one can use a purely abelian methodology to determine the effect of the fractional instantons cut by the plane on the expectation value of the Wilson loop. After all they are neither thin nor abelian. Our naive estimate done in Ref. [24] incorporated these effects by applying a certain reduction factor  $0 < x < 1$  to the size of the fractionals making the relation  $\sigma = 2x^2 l_I^2 \times \rho_{4D}$ . This implies a loss of predictive power although  $x$  is expected not to depend on the lattice spacing. One can envisage a possible independent determination of  $x$  in the fashion presented in Ref. [70], namely creating a configuration as a gas of fractional instantons and measuring the string tension in it.

## 6 Conclusions and future prospects

In this paper, we have explored the evolution of the SU(2) Yang-Mills system living in a  $T_2 \times R^2$  space-time as a function of the size of the 2-torus  $l_s$ . Due to the twisted boundary conditions, the torus is permeated by one unit of 't Hooft flux which prevents the system from breaking the  $Z_2 \times Z_2$  center symmetry at small torus sizes. In this regime one expects that many long-range properties of the system are well-explained by semiclassical methods. In particular, this is given by a gas made of certain local solutions of the classical equations of motion discovered many years ago in Ref. [48] and named vortex-like fractional

instantons. These objects extend over the  $T_2$  torus and are localized in the  $R^2$  plane. Thus, the gas is actually a two-dimensional one. We have explained the semiclassical expectations on the properties of this gas and its implications on global observables of the system such as the string tension or the topological charge density. We have then made a very extensive investigation of the system using lattice gauge theory methods. In particular, we have Monte Carlo generated many configurations, covering a large range of lattice sizes and lattice couplings, in order to test both the semiclassical behaviour of the lattice system as well as its continuum limit. The results presented in Sec. 4 confirm that for torus linear sizes of 0.2-0.6 fermi ( $l_s\sqrt{\sigma} \in [0.09, 0.27]$ ) the system behaves as expected. The density of objects matches closely the predictions of the theory and allows the determination of a basic parameter measuring the strength of quantum fluctuations around the solution. The parameter scales according to the predictions of the beta function of the system confirming that the behaviour is actually a continuum result. Particularly interesting is the evolution of the string tension as a function of the torus size. The Wilson loop around a single vortex-like fractional instanton gives -1, and hence it behaves as a center-vortex. Thus in the dilute situation the system amounts to a two-dimensional  $Z_2$  gauge theory, which is a confining theory with a string tension given by twice the density of the gas. We call this limit the thin-abelian-vortex approximation (TAVA). In our case the vortices have a size, within which the solution reveals its non-abelian character. This produces alterations for small Wilson loops and higher densities that our results exhibit. For low densities the gas displays the expected properties of a Poissonian gas not only in the number-count but also in the spatial distribution.

The previous results have been obtained after applying gradient flow to the Monte Carlo configurations. This process erases short distance fluctuations up to a distance scale called smearing radius. We have chosen this radius of the order of the size of the fractional instanton solution, allowing its easy identification but without alter the distribution of these objects at larger scales. The methodology allows the obtention of smooth images of the configurations giving rise to spectacular videos, which we make available in our supplementary material.

We have also described in the previous section some results obtained for larger torus sizes ( $l_s > 0.6$  fermi). At these sizes the gas stops to be dilute and the semiclassical analysis is far more complicated. Understanding the transition to infinite volume is crucial to relate the physical insight and understanding achieved in our study on the origin of properties such as Confinement to those that hold at  $T=0$  in the infinite system. An important hint is that the value of the string tension attained at the edge of the semiclassical regime is very close to the one known to hold at infinite volume. This is the same type of finding that was obtained many years ago [23, 67] when following a similar strategy within a  $T_3 \times R$  geometry rather than our  $T_2 \times R^2$  path. In that case the semiclassical description is given in terms of a one-dimensional gas of kink-like fractional instantons which play a crucial role in restoring the center-symmetry and generating a non-zero string tension. The search for an explanation led to the proposal of a model of the Yang-Mills vacuum basically describable as a fractional instanton liquid model [25, 71]. The 2D gas develops into a 4D liquid whose characteristic scales are given by physical values not involving the size of space. In this

way the full 4D rotational invariance is recovered and the boundary conditions become irrelevant. This becomes an updated version of the scenario proposed many years ago in Ref. [72] but with the singular merons being replaced by bona-fide smooth solutions of the classical equations of motion: fractional instantons. Exploring this possibility with our methods is very appealing. However, there are considerable improvements that have to be implemented to achieve this goal. In the present work the identification of objects is greatly simplified by the fact that the size is dictated by the geometry and the relevant location is two-dimensional. Furthermore, the gradient flow method could alter the shapes and distribution given that at higher densities the size of the objects and the distances among them have similar values. There are known ways to achieve ultraviolet noise reduction which are less distortive than the Wilson flow method, mostly employed in our present paper. Unfortunately, they involve a considerable upgrade in the resources needed. In our opinion an investigation of the larger sizes should incorporate all these new methods to be really effective. Our plan is to start working along this direction, but its completion will probably take some time.

It is important to emphasize that our results do not necessarily imply that vortices underlie the Confinement property in the infinite volume theory. The vortex-like structure is enforced by the particular choice of geometry used. In the same way the  $T_3 \times R$  geometry led to similar conclusions, but the structure of the semiclassical objects was very different (kink-like FI). Similarly an  $S_1 \times R$  geometry leads naturally to calorons and monopoles. Several recent works have studied how to interpolate among different geometries [38, 73, 74]. In this respect geometry plays a similar (biasing) role to gauge fixing in more traditional lattice studies of confinement [75]. In our opinion, the detailed structure of the fractional instanton liquid is largely unknown and there are at present no strong reasons to believe that they are predominantly arranged into 0-1-2-3-4 dimensional substructures. What is crucial, with respect to the abelian-like gauge fixing arguments, is that these objects carry topological charge and are locally fully-fledged solutions of the non-abelian Yang-Mills equations of motion.

There are other possible extensions of our work which can be addressed and that we plan to consider. A very basic one is going over to larger number of colours  $N$ . One of the nice features of the fractional instanton scenario is that their semiclassical weight survives the large  $N$  limit. A few tests have been done and included in the present paper. This has many attractive features. The generalization of the vortex-like fractional instantons to higher  $N$  are known [76]. The objects are wider and easier to distinguish from ordinary instantons. Furthermore, the proportion of instantons to fractional instantons is expected to drop considerably. Other authors have also conducted studies of different nature centered on the SU(3) case [77, 78].

## Acknowledgments

G. B. and I.S. are funded by the Deutsche Forschungsgemeinschaft (DFG) under Grant No. 432299911 and 431842497. A.G-A acknowledges support by the Spanish Research Agency (Agencia Estatal de Investigación) through the grant IFT Centro de Excelencia

Severo Ochoa CEX2020-001007-S, funded by MCIN/AEI/10.13039/501100011033, and by grant PID2021-127526NB-I00, funded by MCIN/AEI/10.13039/501100011033 and by “ERDF A way of making Europe”. Part of the computing time for this project has been provided by the compute cluster ARA of the University of Jena. The authors gratefully acknowledge the Gauss Centre for Supercomputing e. V. ([www.gauss-centre.eu](http://www.gauss-centre.eu)) for funding this project by providing computing time on the GCS Supercomputer SuperMUC-NG at Leibniz Supercomputing Centre ([www.lrz.de](http://www.lrz.de)).

## References

- [1] G. 't Hooft, *A Property of Electric and Magnetic Flux in Nonabelian Gauge Theories*, *Nucl. Phys. B* **153** (1979) 141–160.
- [2] G. 't Hooft, *Confinement and Topology in Nonabelian Gauge Theories*, *Acta Phys. Austriaca Suppl.* **22** (1980) 531–586.
- [3] G. 't Hooft, *Aspects of Quark Confinement*, *Phys. Scripta* **24** (1981) 841–846.
- [4] M. Luscher, *A New Method to Compute the Spectrum of Low Lying States in Massless Asymptotically Free Field Theories*, *Phys. Lett. B* **118** (1982) 391–394.
- [5] M. Luscher and G. Munster, *Weak Coupling Expansion of the Low Lying Energy Values in the  $SU(2)$  Gauge Theory on a Torus*, *Nucl. Phys. B* **232** (1984) 445.
- [6] M. Luscher, *Some Analytic Results Concerning the Mass Spectrum of Yang-Mills Gauge Theories on a Torus*, *Nucl. Phys. B* **219** (1983) 233–261.
- [7] P. van Baal and J. Koller, *Finite Size Results for  $SU(3)$  Gauge Theory*, *Phys. Rev. Lett.* **57** (1986) 2783.
- [8] J. Koller and P. van Baal,  *$SU(2)$  Spectroscopy in Intermediate Volumes*, *Phys. Rev. Lett.* **58** (1987) 2511.
- [9] J. Koller and P. van Baal, *A Nonperturbative Analysis in Finite Volume Gauge Theory*, *Nucl. Phys. B* **302** (1988) 1–64.
- [10] A. Gonzalez Arroyo and C. P. Korthals Altes, *The Spectrum of Yang-Mills Theory in a Small Twisted Box*, *Nucl. Phys. B* **311** (1988) 433–449.
- [11] D. Daniel, A. Gonzalez-Arroyo, C. P. Korthals Altes and B. Soderberg, *Energy Spectrum of  $SU(2)$  Yang-Mills Fields With Space - Like Symmetric Twist*, *Phys. Lett. B* **221** (1989) 136–142.
- [12] D. Daniel, A. Gonzalez-Arroyo and C. P. Korthals Altes, *The Energy levels of lattice gauge theory in a small twisted box*, *Phys. Lett. B* **251** (1990) 559–566.
- [13] B. A. Berg and A. H. Billoire, *Pure Lattice Gauge Theory in Intermediate Volumes. 1.*, *Phys. Rev. D* **40** (1989) 550.
- [14] P. W. Stephenson and M. Teper, *Glueball Masses and the String Tension in  $SU(2)$  Lattice Gauge Theory With Twisted Boundary Conditions*, *Nucl. Phys. B* **327** (1989) 307–322.
- [15] A. Gonzalez-Arroyo, J. Jurkiewicz and C. P. Korthals-Altes, *Ground State Metamorphosis for Yang-Mills Fields on a Finite Periodic Lattice*, pp. 339–358. Springer US, Boston, MA, 1983.
- [16] A. Coste, A. Gonzalez-Arroyo, J. Jurkiewicz and C. P. Korthals Altes, *Zero Momentum Contribution to Wilson Loops in Periodic Boxes*, *Nucl. Phys. B* **262** (1985) 67–94.

- [17] T. Eguchi and H. Kawai, *Reduction of Dynamical Degrees of Freedom in the Large  $N$  Gauge Theory*, *Phys. Rev. Lett.* **48** (1982) 1063.
- [18] G. Bhanot, U. M. Heller and H. Neuberger, *The Quenched Eguchi-Kawai Model*, *Phys. Lett. B* **113** (1982) 47–50.
- [19] A. Gonzalez-Arroyo and M. Okawa, *The Twisted Eguchi-Kawai Model: A Reduced Model for Large  $N$  Lattice Gauge Theory*, *Phys. Rev. D* **27** (1983) 2397.
- [20] M. Garcia Perez, A. Gonzalez-Arroyo and B. Soderberg, *Minimum Action Solutions for  $SU(2)$  Gauge Theory on the Torus With Nonorthogonal Twist*, *Phys. Lett. B* **235** (1990) 117–123.
- [21] M. Garcia Perez and A. Gonzalez-Arroyo, *Numerical study of Yang-Mills classical solutions on the twisted torus*, *J. Phys. A* **26** (1993) 2667–2678, [[hep-lat/9206016](#)].
- [22] RTN collaboration, M. Garcia Perez et al., *Instanton like contributions to the dynamics of Yang-Mills fields on the twisted torus*, *Phys. Lett. B* **305** (1993) 366–374, [[hep-lat/9302007](#)].
- [23] M. Garcia Perez, A. Gonzalez-Arroyo and P. Martinez, *From perturbation theory to confinement: How the string tension is built up*, *Nucl. Phys. B Proc. Suppl.* **34** (1994) 228–230, [[hep-lat/9312066](#)].
- [24] A. Gonzalez-Arroyo and P. Martinez, *Investigating Yang-Mills theory and confinement as a function of the spatial volume*, *Nucl. Phys. B* **459** (1996) 337–354, [[hep-lat/9507001](#)].
- [25] A. Gonzalez-Arroyo, P. Martinez and A. Montero, *Gauge invariant structures and confinement*, *Phys. Lett. B* **359** (1995) 159–165, [[hep-lat/9507006](#)].
- [26] A. Gonzalez-Arroyo, *On the fractional instanton liquid picture of the Yang-Mills vacuum and Confinement*, [2302.12356](#).
- [27] V. P. Nair and R. D. Pisarski, *Fractional topological charge in  $SU(N)$  gauge theories without dynamical quarks*, *Phys. Rev. D* **108** (2023) 074007, [[2206.11284](#)].
- [28] M. Ünsal, *Strongly coupled QFT dynamics via TQFT coupling*, *JHEP* **11** (2021) 134, [[2007.03880](#)].
- [29] E. Poppitz, T. Schäfer and M. Ünsal, *Universal mechanism of (semi-classical) deconfinement and theta-dependence for all simple groups*, *JHEP* **03** (2013) 087, [[1212.1238](#)].
- [30] E. Poppitz, T. Schäfer and M. Ünsal, *Continuity, Deconfinement, and (Super) Yang-Mills Theory*, *JHEP* **10** (2012) 115, [[1205.0290](#)].
- [31] M. M. Anber, E. Poppitz and B. Teeple, *Deconfinement and continuity between thermal and (super) Yang-Mills theory for all gauge groups*, *JHEP* **09** (2014) 040, [[1406.1199](#)].
- [32] G. Bergner, S. Piemonte and M. Ünsal, *Adiabatic continuity and confinement in supersymmetric Yang-Mills theory on the lattice*, *JHEP* **11** (2018) 092, [[1806.10894](#)].
- [33] M. Ünsal and L. G. Yaffe, *Center-stabilized Yang-Mills theory: Confinement and large  $N$  volume independence*, *Phys. Rev. D* **78** (2008) 065035, [[0803.0344](#)].
- [34] M. Shifman and M. Ünsal, *QCD-like Theories on  $R(3) \times S(1)$ : A Smooth Journey from Small to Large  $r(S(1))$  with Double-Trace Deformations*, *Phys. Rev. D* **78** (2008) 065004, [[0802.1232](#)].
- [35] E. Poppitz, *Notes on Confinement on  $R^3 \times S^1$ : From Yang–Mills, Super–Yang–Mills, and QCD (adj) to QCD(F)*, *Symmetry* **14** (2022) 180, [[2111.10423](#)].

- [36] Y. Tanizaki and M. Ünsal, *Center vortex and confinement in Yang–Mills theory and QCD with anomaly-preserving compactifications*, *PTEP* **2022** (2022) 04A108, [[2201.06166](#)].
- [37] Y. Hayashi and Y. Tanizaki, *Semiclassics for the QCD vacuum structure through  $T^2$ -compactification with the baryon- $\bar{t}$  Hooft flux*, *JHEP* **08** (2024) 001, [[2402.04320](#)].
- [38] Y. Hayashi and Y. Tanizaki, *Unifying Monopole and Center Vortex as the Semiclassical Confinement Mechanism*, *Phys. Rev. Lett.* **133** (2024) 171902, [[2405.12402](#)].
- [39] I. Soler, G. Bergner and A. Gonzalez-Arroyo, *Fractional instantons and Confinement: first results on a  $T_2 \times R^2$  roadmap*, *PoS LATTICE2024* (2025) 408, [[2502.09463](#)].
- [40] J. Zinn-Justin, *Quantum field theory and critical phenomena*, *Int. Ser. Monogr. Phys.* **113** (2002) 1–1054.
- [41] G. V. Dunne and M. Ünsal, *Uniform WKB, Multi-instantons, and Resurgent Trans-Series*, *Phys. Rev. D* **89** (2014) 105009, [[1401.5202](#)].
- [42] G. V. Dunne and M. Ünsal, *New Nonperturbative Methods in Quantum Field Theory: From Large- $N$  Orbifold Equivalence to Bions and Resurgence*, *Ann. Rev. Nucl. Part. Sci.* **66** (2016) 245–272, [[1601.03414](#)].
- [43] I. Aniceto, G. Basar and R. Schiappa, *A Primer on Resurgent Transseries and Their Asymptotics*, *Phys. Rept.* **809** (2019) 1–135, [[1802.10441](#)].
- [44] G. 't Hooft, *Computation of the Quantum Effects Due to a Four-Dimensional Pseudoparticle*, *Phys. Rev. D* **14** (1976) 3432–3450.
- [45] A. Coste, A. Gonzalez-Arroyo, C. P. Korthals Altes, B. Soderberg and A. Tarancon, *Finite Size Effects and Twisted Boundary Conditions*, *Nucl. Phys. B* **287** (1987) 569–588.
- [46] M. Luscher and P. Weisz, *Efficient Numerical Techniques for Perturbative Lattice Gauge Theory Computations*, *Nucl. Phys. B* **266** (1986) 309.
- [47] A. A. Belavin, A. M. Polyakov, A. S. Schwartz and Y. S. Tyupkin, *Pseudoparticle Solutions of the Yang-Mills Equations*, *Phys. Lett. B* **59** (1975) 85–87.
- [48] A. Gonzalez-Arroyo and A. Montero, *Selfdual vortex - like configurations in  $SU(2)$  Yang-Mills theory*, *Phys. Lett. B* **442** (1998) 273–278, [[hep-th/9809037](#)].
- [49] E. B. Bogomolny, *Stability of Classical Solutions*, *Sov. J. Nucl. Phys.* **24** (1976) 449.
- [50] M. K. Prasad and C. M. Sommerfield, *An Exact Classical Solution for the 't Hooft Monopole and the Julia-Zee Dyon*, *Phys. Rev. Lett.* **35** (1975) 760–762.
- [51] A. Gonzalez-Arroyo, “On the  $su(2)$  vortex-like fractional instanton solution; (manuscript in preparation).”.
- [52] G. Bergner, A. González-Arroyo and I. Soler, *Identifying topological structures with adjoint mode filtering*, *JHEP* **05** (2024) 048, [[2401.16913](#)].
- [53] C. Allton, M. Teper and A. Trivini, *On the running of the bare coupling in  $SU(N)$  lattice gauge theories*, *JHEP* **07** (2008) 021, [[0803.1092](#)].
- [54] J. Groeneveld, J. Jurkiewicz and C. P. Korthals Altes, *LOCAL ORDER PARAMETER IN TWISTED GAUGE FIELDS*, *Phys. Lett. B* **92** (1980) 312–314.
- [55] J. Groeneveld, J. Jurkiewicz and C. P. Korthals Altes, *Twist as a Probe for Phase Structure*, *Phys. Scripta* **23** (1981) 1022.

- [56] A. Gonzalez-Arroyo and R. Kirchner, *Adjoint modes as probes of gauge field structure*, *JHEP* **01** (2006) 029, [[hep-lat/0507036](#)].
- [57] M. Garcia Perez, A. Gonzalez-Arroyo and A. Sastre, *Adjoint fermion zero-modes for  $SU(N)$  calorons*, *JHEP* **06** (2009) 065, [[0905.0645](#)].
- [58] M. Lüscher, *Properties and uses of the Wilson flow in lattice QCD*, *JHEP* **08** (2010) 071, [[1006.4518](#)].
- [59] C. Alexandrou, A. Athenodorou and K. Jansen, *Topological charge using cooling and the gradient flow*, *Phys. Rev. D* **92** (2015) 125014, [[1509.04259](#)].
- [60] R. Narayanan and H. Neuberger, *Infinite  $N$  phase transitions in continuum Wilson loop operators*, *JHEP* **03** (2006) 064, [[hep-th/0601210](#)].
- [61] M. Teper, *Instantons in the Quantized  $SU(2)$  Vacuum: A Lattice Monte Carlo Investigation*, *Phys. Lett. B* **162** (1985) 357–362.
- [62] V. G. Bornyakov, E. M. Ilgenfritz, B. V. Martemyanov and M. Müller-Preussker, *Dyons near the transition temperature in lattice QCD*, *Phys. Rev. D* **93** (2016) 074508, [[1512.03217](#)].
- [63] Y. Tanizaki, A. Tomiya and H. Watanabe, *Lattice gradient flows (de-)stabilizing topological sectors*, [2411.14812](#).
- [64] M. Garcia Perez, A. Gonzalez-Arroyo, J. R. Snippe and P. van Baal, *Instantons from over-improved cooling*, *Nucl. Phys. B* **413** (1994) 535–552, [[hep-lat/9309009](#)].
- [65] P. J. Braam and P. van Baal, *Nahm’s Transformation for Instantons*, *Commun. Math. Phys.* **122** (1989) 267.
- [66] P. de Forcrand, M. Garcia Perez and I.-O. Stamatescu, *Topology of the  $SU(2)$  vacuum: A Lattice study using improved cooling*, *Nucl. Phys. B* **499** (1997) 409–449, [[hep-lat/9701012](#)].
- [67] RTN collaboration, M. Garcia Perez et al., *Instanton like contributions to the dynamics of Yang-Mills fields on the twisted torus*, *Phys. Lett. B* **305** (1993) 366–374, [[hep-lat/9302007](#)].
- [68] M. Luscher, K. Symanzik and P. Weisz, *Anomalies of the Free Loop Wave Equation in the WKB Approximation*, *Nucl. Phys. B* **173** (1980) 365.
- [69] A. Gonzalez-Arroyo and M. Okawa, *The string tension from smeared Wilson loops at large  $N$* , *Phys. Lett. B* **718** (2013) 1524–1528, [[1206.0049](#)].
- [70] A. Gonzalez-Arroyo and A. Montero, *Do classical configurations produce confinement?*, *Phys. Lett. B* **387** (1996) 823–828, [[hep-th/9604017](#)].
- [71] A. Gonzalez-Arroyo and P. Martinez, *Investigating Yang-Mills theory and confinement as a function of the spatial volume*, *Nucl. Phys. B* **459** (1996) 337–354, [[hep-lat/9507001](#)].
- [72] C. G. Callan, Jr., R. F. Dashen and D. J. Gross, *A Mechanism for Quark Confinement*, *Phys. Lett. B* **66** (1977) 375–381.
- [73] E. Poppitz and F. D. Wandler, *Gauge theory geography: charting a path between semiclassical islands*, *JHEP* **02** (2023) 014, [[2211.10347](#)].
- [74] F. D. Wandler, *Numerical fractional instantons in  $SU(2)$ : center vortices, monopoles, and a sharp transition between them*, [2406.07636](#).
- [75] J. Ambjorn, J. Giedt and J. Greensite, *Vortex structure versus monopole dominance in Abelian projected gauge theory*, *JHEP* **02** (2000) 033, [[hep-lat/9907021](#)].

- [76] A. Montero, *Study of SU(3) vortex - like configurations with a new maximal center gauge fixing method*, *Phys. Lett. B* **467** (1999) 106–111, [[hep-lat/9906010](#)].
- [77] E. Itou, *Fractional instanton of the SU(3) gauge theory in weak coupling regime*, *JHEP* **05** (2019) 093, [[1811.05708](#)].
- [78] M. M. Anber, A. A. Cox and E. Poppitz, *On the moduli space of multi-fractional instantons on the twisted  $\mathbb{T}^4$* , [2504.06344](#).

## A Dependence of the distributions on gradient flow parameters

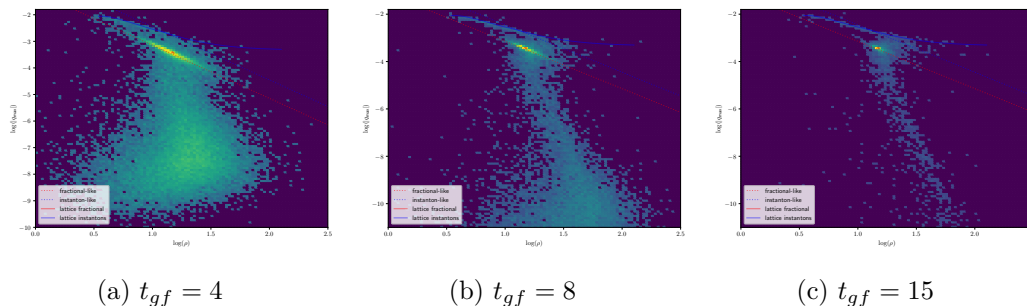


**Figure 22.** Density plot of the fit parameters obtained with same parameters as Fig. 5 but for different gradient flow times  $t_{gf}$ . Only a subset of the configuration has been considered.

The distribution of fractional instantons depends on the gradient flow time and on the choice of the lattice action in the gradient flow. For a subset of the total configurations, we have repeated the analysis at different flow times  $t_{gf}$ . The result is shown in Fig. 22 with an increased scale of the y-axis to show the noise level at small  $q_{\max}$ .

At small  $t_{gf}$ , the level of the background noise indicated by the contribution at very small  $q_{\max}$  is much higher. In addition the single peak of the fractional instanton gets blurred into a wider stripe by the noise. In these examples, the noise is even at  $t_{gf} = 4$  well separated from the fractional instanton peak, but at larger  $l_s$  and smaller  $t_{gf}$  the identification becomes more ambiguous. Increasing the flow time, the noise gets reduced and the semiclassical features become clearer. At the same time, however, fractional instanton anti-instanton pairs are annihilated and the tail of the distribution is reduced.

We have also tested the overimproved flow as an alternative to the standard gradient flow with the Wilson action. In the regime at small  $l_s$  and the specific flow times considered in our current analysis, there is no major difference between the two flow types. However, we expect a relevant difference towards larger  $l_s$ . One very small effect is that the instanton contributions are slightly shifted towards larger radius with the overimproved flow.

## B Distribution of fit parameters at larger $N_c$ (SU(3) and SU(4))

We have investigated the topological densities on  $T_2 \times R^2$  also at larger  $N_c$  for  $SU(N_c)$  gauge theories. In the current work, we don't aim for a complete analysis of these cases,

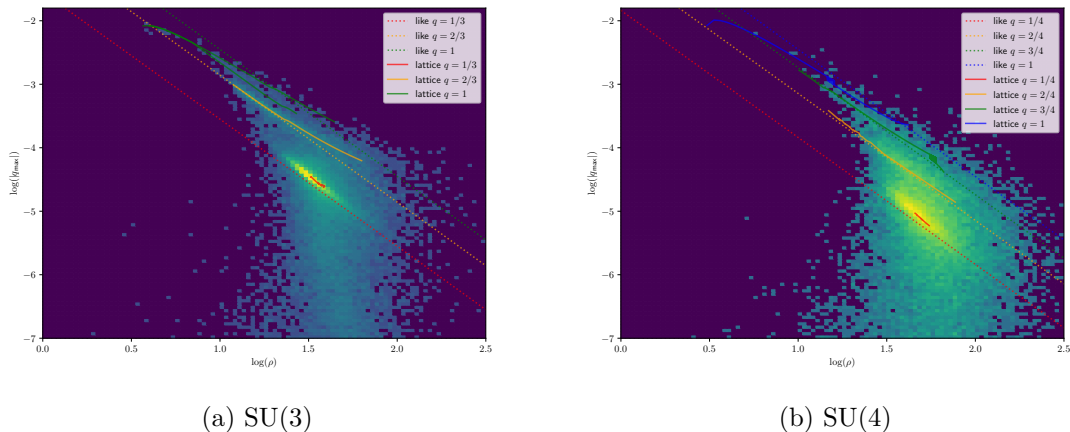


**Figure 23.** Density plot of the fit parameters obtained in case of SU(3) and SU(4) Yang-Mills theory. In both cases a  $N_s = 6$ ,  $N_r = 64$  lattice configuration.  $\beta = 6.3$  for SU(3) and  $\beta = 11.5$  for SU(4). In the case of SU(3) we have added two possible deformations of instantons as “lattice  $q = 1$ ” and their evolution with the gradient flow.

but we want to provide some of the results in order to discuss possible differences. The larger  $N_c$  cases allow for several choices of the twist. We focus here on the same twist as in the SU(2) case.

Semiclassical configurations are generated at large  $\beta$  and sufficient gradient flow. Using appropriate boundary conditions one can generate examples for the different objects with fractional  $Q_I$ . The semiclassical configurations can be deformed using different types of gradient flow.

A significant difference compared to SU(2) are the additional possible  $Q_I < 1$  configurations apart from the minimal  $\frac{1}{N_c}$  topological charge. In the case of SU(3), for example, there are additional semiclassical objects with topological charge  $2/3$ . The instantons have, consequently, several possibilities to be decomposed into these objects. In a distribution at small  $l_s$ , which consists mostly out of  $Q = 1/N_c$  fractional instantons, the  $Q = 1$  contributions are less likely to be generated.

### C Further characteristics of fractional instanton distribution

We have investigated further observables in order to characterize the fractional instanton distributions. A more detailed discussion of fractional instanton solutions on  $T_2 \times R^2$  will be presented in a further publication and we therefore only briefly mention some properties, which can be investigated on the lattice.

One example are the Polyakov loops in the two short directions  $P_0(x_1, x_2, x_3)$  and  $P_1(x_0, x_2, x_3)$ . At each point in  $R^2$  ( $x_2, x_3$ ) we take the value at the maximum of its modulus. Choosing  $x_1$  or  $x_2$  such that  $|P_0|$  or  $|P_1|$  are maximized gives a two-dimensional distribution of two numbers, a vector field. We represent it by the modulus and the angle  $\phi$  of the corresponding vector. Semiclassics predicts that the vector is maximized at the center of each fractional instanton, which means that  $|P_0| = |P_1| = 2$ . These provide four

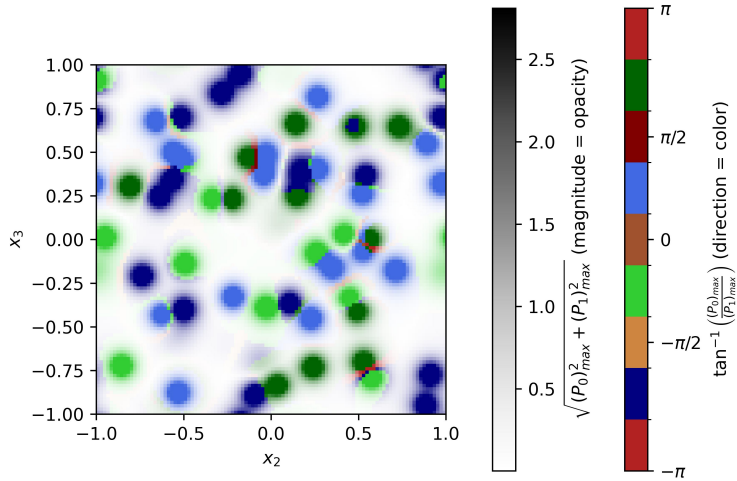
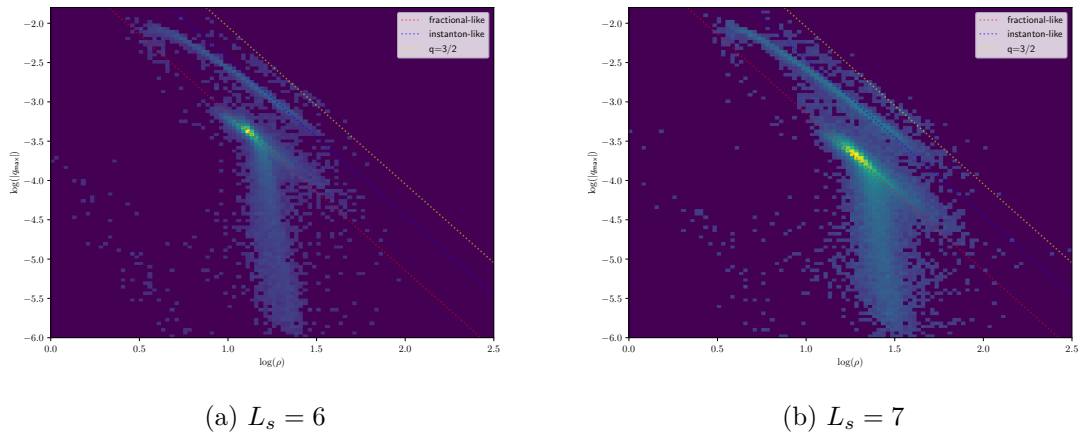


**Figure 24.** Polyakov loop at  $N_s = 6$ ,  $\beta = 2.6$ . Same configuration as Fig 4a



(a)  $L_s = 6$

(b)  $L_s = 7$

**Figure 25.** Fit of the peak contributions at  $L_s = 6, 7$ ;  $L_r = 104$ ;  $\beta = 2.6$ ; and  $t_{gf} = 15$ . In contrast to the previous presentation in Fig. 5, all fit peaks are included in a single fit.

independent orientations at the center points depending on the relative sign of  $P_1$  and  $P_2$ :  $(+, +)$  corresponding to  $\phi = \pi/4$ ;  $(+, -)$  corresponding to  $\phi = -\pi/4$ ;  $(-, -)$  corresponding to  $\phi = -3\pi/4$ ;  $(-, +)$  corresponding to  $\phi = 3\pi/4$ . Fig. 24 shows that this is indeed in agreement with the results.

## D Improved fit of fractional instanton distributions

We have already tested methods to improve the fit of the fractional instanton contributions. It is possible to include the linear superposition of several objects in a single fit approach. In this way, one considers all of the peaks in a single fit. We have done first tests on such

kind of approaches and the results are illustrated by Fig. 25. Note that we have considered only a single radius parameter  $\rho = \rho_2 = \rho_3$  and considered only the part of the distribution above the noise level. The results indicate a clearer separation of the different topological contributions. However, it seems that more advanced methods are required in order to clarify the picture at large  $l_s$ .

## E Extra tables

$L_s$	$L_r$	$\beta$
3	104	2.6
4	104	2.4
4	104	2.5
4	104	2.55
4	104	2.6
4	104	2.65
4	104	2.7
5	104	2.4
5	104	2.5
5	104	2.55
5	104	2.6
5	104	2.65
5	104	2.7
6	104	2.4
6	104	2.5
6	104	2.55

$L_s$	$L_r$	$\beta$
6	104	2.6
6	104	2.65
6	104	2.7
7	104	2.4
7	104	2.5
7	104	2.55
7	104	2.6
7	104	2.65
7	104	2.7
8	104	2.6
8	104	2.65
8	104	2.7
8	64	2.55
9	104	2.6
9	104	2.65
9	104	2.7

$L_s$	$L_r$	$\beta$
9	104	2.8
9	64	2.55
10	104	2.6
10	104	2.65
10	104	2.7
10	64	2.55
10	64	2.6
11	64	2.6
12	64	2.6
13	64	2.6
14	104	2.6
18	104	2.7
20	64	2.6
30	64	2.6

**Table 2.** Complete collection of all runs relevant for our Monte-Carlo simulations summarized in Tab. 1.